Hair Bundle Degeneration is a Key Contributor to Age-Related Vestibular Dysfunction

Samadhi Kulasooriya[1*], Huizhan Liu[1], Sarath Vijayakumar[1], Celia Bloom[1], Shu Tu[1], Benjamin J. Borgmeier[1], Mi Zhou[1], Litao Tao[1], Bechara Kachar[2], David Z. He[1*]

[1]Department of Biomedical Science, School of Medicine, Creighton University, Omaha, Nebraska, USA

[2]Laboratory of Cell Structure and Dynamics, National Institute of Deafness and Other Communication Disorders, National Institutes of Health, Bethesda, Maryland, USA

Corresponding authors:

David Z. He (DavidHe@creighton.edu)

Samadhi Kulasooriya (SamadhiKulasooriya@creighton.edu)

Teaser: Hair bundle degeneration and age-related vestibular dysfunction

Abstract

Age-related vestibular dysfunction (ARVD) is a prevalent, debilitating condition in the elderly. The etiology and molecular mechanisms are poorly understood. We focused on mechanosensitive hair cells (HCs) as they are vulnerable to aging. Using single-cell RNA-seq transcriptomes of young and old mouse vestibular HCs, we show that aging vestibular HCs display both universal molecular signatures, such as genomic instability, mitochondrial dysfunction, and impaired proteostasis, and cell type-specific changes associated with deterioration of hair bundles and mechanotransduction. In alignment with transcriptomic findings, imaging and electrophysiological recordings from aged vestibular sensory epithelia confirmed the degeneration of the hair bundles and a reduction in mechanotransduction. Importantly, this deterioration of hair bundles and vestibular function precedes HC loss, highlighting impaired mechanotransduction as a key contributor to ARVD. Furthermore, molecular and cellular changes associated with aging signatures are less pronounced in vestibular HCs than in cochlear HCs, underscoring tissue-specific age-related differences between the two sensory epithelia in the inner ear.

Introduction

Aging research has experienced unprecedented advances in recent years, revealing that genetic and molecular processes conserved through evolution may partially govern the pace of aging (*1*). Aging is the progressive deterioration of physiological integrity, leading to impaired function and enhanced vulnerability to disease and death. The molecular processes of aging are characterized by the universal hallmarks of aging, including increased cellular senescence, genomic instability, epigenetic alterations, mitochondrial dysfunction, loss of proteostasis, and inflammaging (*1*, *2*). The interconnected and interdependent nature of these processes leads to slow age-related structural changes and functional decline. Similar to other sensory organs, biological aging negatively impacts the inner ear, resulting in age-related hearing loss (ARHL) and vestibular dysfunction (ARVD). While numerous studies have focused on ARHL, ARVD remains relatively understudied, partially due to its multifaceted etiology (*3*–*8*). ARVD is characterized by the gradual loss of bilateral vestibular function accompanied by interruptions to visual and proprioceptive inputs. The damaging impact of age-related vestibular sensory decline manifests itself in an exponential increase in geriatric dizziness and injurious/fatal falls (*9*). According to the National Center for Health Statistics and National Institutes of Health, the prevalence of ARVD in the US is 75.3%. It is the 6th leading cause of death and accounts for 50% of all accidental deaths among the elderly population (*5*, *10*).

While the central neural pathways in the vestibular system play a role in ARVD, age-related degeneration of vestibular hair cells (HCs) and neurons in the vestibular periphery contributes to ARVD (*11*). The vestibular system plays a crucial role in sensing the direction, acceleration, and spatial orientation of the head in response to gravity to maintain the upright posture and balance of the body. It consists of three crista ampullaris that detect the angular motions and two otolith organs (utricle and saccule) that detect linear motions of the head (*12*). Vestibular sensory epithelia consist of two types of mechanosensitive HCs, type I and type II. HCs convert mechanical stimuli into electrical signals. Mechanotransduction, the first step in the vestibular signal processing, is mediated by the mechanotransduction apparatus in the hair bundle comprising tightly linked stereocilia and a kinocilium (*13*, *14*). Therefore, damage or degeneration of hair bundles will lead to vestibular functional decline (*11*, *13*–*16*). Interestingly, studies from human and murine models indicate an earlier and more pronounced auditory functional and morphological decline compared to the vestibular system, highlighting tissue-specific differences between these sensory organs (*7*, *9*). However, molecular mechanisms driving these divergent aging processes remain unknown. This fundamental lack of understanding of the molecular basis of vestibular aging remains a significant barrier to developing targeted therapeutic interventions to mitigate ARVD (*17*).

While previous studies have examined age-related physiological and morphological changes in the vestibular system, no studies have been performed to assess age-related changes of vestibular HCs at the molecular level. Therefore, it is still unclear whether vestibular HCs follow the universal blueprint of aging as seen in neurons and cochlear HCs, and whether vestibular HCs also exhibit cell-type-specific aging signatures. In the current study, we comprehensively examined the aging of the vestibular system across functional, morphological, and molecular levels. Transcriptomic studies have been at the forefront of revealing the molecular underpinnings of development, aging, and disease conditions in model organisms and humans. Utilizing single-cell RNA sequencing (scRNA-seq), we characterized universal and cell-type-specific aging signatures in vestibular HCs from young and aged mice. The cell type-specific aging signatures are primarily associated with the degeneration of hair bundles and the mechanotransduction apparatus. Concordant with that, electrophysiology and imaging revealed that vestibular functional decline and bundle degeneration precede HC loss, highlighting the degeneration of the hair bundles as a key contributor to ARVD. The comparison between vestibular and cochlear HCs shows that the age-related molecular and cellular changes are less pronounced in vestibular HCs than in cochlear HCs, underscoring the subtle differences in aging between the two sensory epithelia in the mammalian inner ear. Our data also provide a foundational transcriptomic resource to advance the understanding of inner ear aging and the development of targeted therapeutic strategies.

Results

Age-related functional and morphological changes in the vestibular HCs

Prior studies have reported various age-related functional and structural changes in the vestibular end organs (*5*, *6*, *18*, *19*). In this study, we utilized CBA/J mice, which exhibit progressive age-related changes in the inner ear in the later stage of life, similar to humans (*20*, *21*). To examine the age-related functional decline in the vestibular system, we measured vestibular sensory evoked potentials (VsEP) from 2-2.5 months (young) and 22-24 months (old) mouse cohorts. This test measures electrical signals generated by the vestibular sensory epithelia in response to rapid linear head accelerations by evaluating sensitivity (threshold), strength of the response (amplitude), and time taken by the signal to reach the recording electrode after stimulus initiation (latency) (*22*, *23*). Consistent with previous findings, our results indicated an age-related decline in the vestibular function, as evidenced by a significant decrease in the response amplitude and an increase in the threshold and latency (Fig.1, A to C). We also measured endolymphatic potential (ELP), which is essential for maintaining the ionic gradient required for mechanotransduction (*24*), and it typically ranges from +1 to +11 mV (*25*–*27*). Our findings revealed no age-related change in ELP, indicating maintenance of a stable electrochemical environment (Fig.1D). Next, we examined the age-related morphological alterations in vestibular HCs. Previous studies have reported an age-related loss of vestibular HCs in both mice and humans (*6*, *16*, *28*, *29*), with more loss of type I HCs than type II HCs (*6*), while some studies indicate no HC loss (*30*). Thus, to re-examine the age-related HC loss, we immunolabeled young and old utricles with HC-specific marker MYO7A and type II HC-specific marker SOX2 (*31*–*33*). Our findings showed no age-related changes in type I and II HC density in the striolar and extrastriolar regions (Fig.1, E and F, fig. S1). Cellular hypertrophy and atrophy are commonly seen in aging cells, including cochlear HCs and neurons (*33*, *34*). To further assess the age-related cytological changes in vestibular HCs, we performed a histological analysis (Fig.1, G to I). While we observed cellular hypertrophy and atrophy in some HCs, there were no significant changes in cell length (Fig.1, H and I).

We utilized high-resolution confocal imaging to examine the age-related changes in the hair bundle. Stereocilia were labeled with phalloidin, and kinocilia were immunostained with anti-acetylated-β-tubulin. We observed signs of stereociliopathy, including complete and partial loss of stereocilia leading to bundle thinning and shortening, and fusion of stereocilia, alongside degeneration of kinocilia (Fig. 2A). While cochlear HCs lose the kinocilia during maturation, vestibular kinocilia are maintained in adult HCs and play a crucial role in hair bundle polarity, determining directional sensitivity and connecting the hair bundle to the overlaying otolithic membrane (*35*, *36*). We observed signs of kinociliary degeneration, including kinocilia fusion (fuses with neighboring kinocilia or stereocilia), and shortening, tip or mid-shaft bulb formation, aberrant looping, and knotting (Fig. 2A). These degenerative changes increased with aging in both the utricle and cristae (Fig. 2B). We also utilized scanning electron microscopy (SEM) to examine the ultrastructure of the hair bundle, and we observed various signs of bundle degeneration (Fig. 2C). Collectively, these findings indicate various age-related changes, particularly in the hair bundle, that may impair mechanotransduction and sensory perception, leading to vestibular functional decline as indicated by VsEP.

Cellular diversity in young and old vestibular end organs

The molecular mechanisms underlying age-related vestibular degeneration are poorly understood (*37*). To unveil this, we conducted single-cell RNA-sequencing (scRNA-seq) of inner ears harvested from 10-week- and 22-month-old CBA/J mice. The sequencing reads were aligned to the mouse reference genome (mm10), followed by standard quality control metrics and downstream processing steps, including dimensional reduction and unsupervised clustering (Fig.3A, fig. S2) (*38*). Cell clusters were annotated based on known marker gene expression and gene signatures (Fig.3, B and C). We examined the cellular diversity in the vestibular sensory epithelia of young and old samples, encompassing type I and II HCs, supporting cells, and blood, neuronal, immune, and epithelial cell populations. HCs were identified based on the expression of markers such as *Pou4f3*, *Myo7a*, *Slc17a8*, and *Otof* (*39*, *40*), and type I and II HC types were differentiated using *Sox2* (*31*, *32*) (Fig.3D, E, G, H). Based on these markers, 698 type I and 129 type II HCs from young samples and 1651 type I and 230 type II HCs from old samples were isolated for the downstream analysis (Fig.3, F and I).

Universal hallmarks of aging

Cellular aging typically follows universal aging programs (*1*, *2*). Prior studies have demonstrated that cochlear HC aging is associated with universal hallmarks such as mitochondrial dysfunction, oxidative stress,

apoptosis, and genomic instability (*17*). Thus, we speculated that aging vestibular HCs may also exhibit universal hallmarks. We aggregated single-cell raw counts to generate pseudobulk expression matrices of young and old vestibular HCs (table S2), and the gene expression levels related to universal hallmarks were analyzed using genes identified from multiple resources as described in the methods (Fig.4A). Cellular senescence is characterized by the permanent cessation of the cell cycle. Senescent cells adopt the characteristic senescence-associated secretory phenotypes (SASP), which exert deleterious effects on cellular function over time and are recognized as a hallmark of cellular aging (*1*, *2*, *41*). Our data indicated a decrease in cell cycle regulators (*Cdk2, Cdk4, Cdk6*), followed by an increase in cyclin-dependent kinase inhibitors (*Cdkn1a, Cdkn1b*), and degradation of cyclins (*Fzr1*), indicating cell cycle arrest. Moreover, we noted an increase in senescence induction (*Ypel3*), a decrease in laminins (*Lmna, Lmnb1*), and enrichment of various SASPs that are involved in inflammation (*Cxcl14, Nfkb2, B2m*), senescence-associated heterochromatic foci (*H3f3a, Hira, Ubn1*), hypoxia, and angiogenesis (*Vegfa, Hif1a, Nos3*), indicating increased senescence in old HCs relative to young HCs. The imbalance between the production and elimination of reactive oxygen species (ROS) results in oxidative stress (*1*, *2*). We observed an increased expression of genes involved in mitochondrial respiration, the major contributor of ROS generation (*Cox4i1, Cox6a1, mt-Co1, mt-Cytb, Ndufs2*), antioxidant response and detoxification (*Mt1, Sod1, Prdx1, Gpx4, Keap1, Nrf1*), mitochondrial fission and fusion (*Fis1, Mfn1, Mfn2*), stress response (*Bcl2, Atf4, Cflar, Hif1a, Atf4, Atf5*) and mitochondrial quality control (*Lonp1, Trap1*), suggesting age-related increase in oxidative stress followed by a compensatory increase in antioxidant mechanisms. In addition, we noticed a decrease in key genes involved in the detoxification of hydrogen peroxide, such as *Gpx1, Prdx1, Sod3*, and *Cat*, indicating partial ROS clearance.

Age-related gradual increase in chronic low-grade inflammation is termed inflammaging (*1*, *2*). We noticed a steady increase in pro-inflammatory genes (*Ptgds, Cxcl14, Ccl12, Il1a, Nfkb1, Jak1, Stat3, Tradd, Fadd, Irak1, Mapk1, Mapk14*) and downregulation of some genes (*Tgfb1, Cxcl12, Tlr3, Tlr4, Myd88, Irak4, Ccl2, Ccl5, Ccl11*), indicating potential maintenance of a prolonged low-grade inflammatory state followed by reduced immune surveillance and response. Epigenetic dysregulation increases with aging (*42*). Our data demonstrated age-related epigenetic alterations, including a reduction in global heterochromatin (*Kdm5a, Kdm6a, Ezh1, Ezh2, Setdb2, Smarcb1*), nucleosome remodeling (*Smarca1, Ino80b, Vps72, Phf8, Chd4, Chd5, Anp32e, Itgb3bp, Ssrp1, Baz2a*), changes in histone marks (*Mll1, Mll3, Setd2, Kdm4a, Hdac3, Hdac4, Ctcf, Cbx3*), global DNA hypomethylation, and CpG hypermethylation (*Dnmt1, Dnmt3b, Tet1, Ezh1, Ezh2*). Age-driven dysregulation of mechanisms involved in protein synthesis, folding, and turnover leads to impaired protein homeostasis, followed by the accumulation of misfolded protein aggregates. We noted the downregulation of genes involved in misfolded/unfolded protein response (*Hspb1, Hspb2, Dnajb5, Dnajb14, Dnajc24, Dnajc5, Vcpip*) and protein turnover (*Ube2e2, Usp38, Uch15, Rnf38, Fbxo31, Fbxw8*), indicating signs of impaired proteostasis.

Reduced DNA repair capability accumulates DNA damage, leading to genome instability with aging (*1*, *2*, *43*). We observed a decrease in the expression of genes involved in DNA damage response (*Trp53, Mdm2, Chek1, and Chek2*) and repair mechanisms (*Rad50, Rad52, Xpc, Xrcc1, Xrcc2, Atr, Atm, Mgmt, Apex1, Recql*), indicating diminished DNA repair in old vestibular HCs. Autophagy is crucial to recycling damaged organelles to maintain cellular homeostasis (*1*, *2*). We noted the enrichment of key genes related to autophagy initiation, autophagosome formation, and progression (*Becn1, Atg12, Atg13, Atg16l1, Atg101, Map1lc3b, Ulk1, Ulk2, Fundc1, Tbk1, Pink1, Sqstm1, Tsc2, Bnip3*). However, we also noted the downregulation of key genes (*Atg5, Atg7, Atg9a, Atg9b, Atg10, Atg14, Prkaa1, Prkaa2, Ambra1, Nrbf2, Lepr, Ppargc1a*) that are involved in autophagosome elongation, autophagy progression, and energy sensing. While this may suggest active regulation of autophagy, there are signs of dysregulation in autophagosome formation and energy sensing. Aging impacts extracellular matrix (ECM) dynamics and intercellular communication (*1*, *2*). Our data indicated a reduction in genes involved in cell-cell adhesion (*Cdh1, Cdh3, Cdh15, Pcdh17, Pcdh9, Pcdhga4, Ptprk, Ptprf*), intercellular communication (*Gja1, Gjb2, Nlgn1, Nlgn2*), ECM interactions and diminished tissue integrity (*Itgb1, Itgav, Itga8, Tjp3, Cldn10, Cldn23*).

We utilized RNAscope *in situ hy*bridization to validate some key markers identified from our analysis (Fig. 4B). Previous studies show that the downregulation of proteostasis regulator, *Hspb1* (encodes Heat-shock protein 27), is associated with ARHL (*44*). Moreover, mutations in *Gjb2* (encodes connexin 26) are associated with genetic deafness accompanied by vestibular dysfunction (*45*). Coinciding with our transcriptomic findings, we noted a significant decrease in *Hspb1* and *Gjb2* in vestibular HCs with biological aging, which may play roles in ARVD. Together, these data indicate that vestibular HC aging follows universal aging programs.

Cell type-specific aging signatures

Previous studies have revealed distinct cell type-specific aging signatures across various tissues (*46–48*). Hence, we examined whether the universal vestibular HC aging programs are accompanied by cell type-specific aging signatures. We performed PCA multivariate analysis to examine the overall age-driven changes in the gene expression in young and old type I and II HCs across our 5 biological replicates. Our results show that the most striking differences in our datasets occur between young and old groups, rather than between type I and II HCs, as evidenced by the 96% variance of principal component 1 (Fig.5A). Next, we assessed the number of unique and shared genes expressed in young and old type I and II HCs. We noted that irrespective of cell type or age, the majority of genes (60.7%) are shared among HCs (Fig.5B). To evaluate the age-related differences between young and old HCs, we conducted a differentially expressed gene (DEG) analysis (Fig.5, C and D). We primarily focused on the genes associated with universal or cell type-specific aging signatures (Fig.5E). Our DEG analysis revealed age-related downregulation of hair bundle-related genes, including *Ush1c, Espn, Cib2, Dynll2, Tubb4b, Actb, Gsn, Calm1, Tekt2, Nudc, Evl, Cfap46,* and *Atp2b2*, most of which are associated with genetic balance disorders and hearing loss (*49–53*). Downregulation of these genes in the vestibular HCs during biological aging may play a crucial role in the development of ARVD and could serve as potential biomarkers. Additionally, many of our top enriched DEGs are linked to universal hallmarks, including oxidative stress (*mt-Co3, mt-Cytb mt-Atp6*), inflammation (*Ptgds*), and epigenetic alterations (*Pifo, Tle5, Chrac1, Gtf2i*) while top downregulated DEGs were associated with proteostasis (*Hsbp1, Hsp90ab1, Cct7, Erp29, Fbxo2, Uba52*), and intercellular communication (*Dctn3, Epcam, Afdn*). Previous studies have suggested that type I HCs are more vulnerable to aging than type II HCs (*9*). While we did not observe significant differences between the two types of HCs at the cellular and molecular levels, we observed some heterogeneity in HC function-related genes among individual HCs (fig. S3). Overall, these findings suggest that vestibular HCs exhibit both universal and cell type-specific aging signatures.

Biological processes associated with old vestibular HCs

To examine the biological relevance of our observed DEGs, we performed gene ontology (GO) enrichment analysis and Kyoto Encyclopedia of Genes and Genomes (KEGG) analysis. We observed a significant downregulation of GO terms and genes related to i) HC structure and functions including sensory perception of stimuli, stereocilia bundle, organization, and cytoskeleton, ii) proteostasis-related processes such as regulation of protein ubiquitination, proper protein folding, and refolding, iii) synapses indicating the age-driven decline of several key functional processes in old HCs (Fig.6, A and B). While kinocilia have long been regarded as a primary cilium, a recent study suggests that mouse and frog vestibular kinocilia possess both primary and motile cilia machinery, exhibiting motility (*54*). Coinciding with this, we noted downregulation of GO-terms and key genes related to kinocilia structure and motility (Fig.6, A to C). We observed a significant downregulation of many genes involved in kinocilia structure and function, such as *Ccdc39, Ccdc40, Ccdc96, Pifo, Gsn, Cfap126, Hydin, Rpsh1, Ttll3, Ttc21a, Cafp45,* as well as those linked to stereocilia and HC function such as *Espn, Ush1c, Pou4f3, Homer2, and Slc17a8*. Many of these genes are linked to ciliopathies, congenital deafness, and balance disorders (*35, 50, 51, 55*).

ARVD is increasingly recognized as a key player in neurodegenerative diseases and cognitive decline, indicating a bidirectional association (*56, 57*). Interestingly, our KEGG pathway analysis of old vestibular HCs revealed significant enrichment of signaling pathways linked to various neurodegenerative diseases, including Alzheimer's (AD), Parkinson's (PD), Huntington's (HD), and amyotrophic lateral sclerosis (ALS), along with an elevated expression of AD/PD (*Apoe, App, Mapt*), HD (*Htt*), ALS, and dementia (*Nefl, Fus, Tardbp, C9orf72*) susceptibility genes (Fig.6, D and E) (*58–61*). Our results suggest that neurons and vestibular HCs exhibit some shared aging patterns, indicating that vestibular HC aging may represent both an associated condition and a potential biomarker for neurodegenerative diseases. These results further emphasize the complex interplay between universal and cell type-specific mechanisms underlying ARVD. Moreover, our GO analysis showed downregulation of biological processes and genes related to proteostasis, such as *Hsp90aa1, Hsp90ab1, Hspa2, Cct7,* and *Dnajb2*. Age-driven dysregulation of proteostasis and subsequent accumulation of protein aggregates lead to the onset of various diseases, including neurodegenerative diseases (*62*).

Next, we assessed the age-related downregulation of key genes identified from our analyses. Concordant with our transcriptomic findings, our experimental validations by RNAscope *in situ* hybridization

and immunostaining showed a significant downregulation of key HC markers at both gene and protein levels (Fig.7, A to D, fig. S4). To examine whether these molecular changes associated with the hair bundle impair mechanotransduction in the old vestibular HCs, we assessed the FM1-43 styryl dye uptake by the vestibular HCs *in vitro*. FM1-43 is a fluorescent dye that rapidly enters HCs via mechanotransduction channels in the hair bundle (*63*). We observed a significant reduction in FM1-43 uptake in both the utricle and crista of old mice (Fig. 7E), indicating compromised mechanotransduction channel activity with aging. To further evaluate HC function *in vivo*, we recorded vestibular microphonic, which reflects HC mechanotransduction and function (*64*). We observed a significant age-associated reduction in the magnitude of vestibular microphonic response in the old mice compared to young mice (Fig. 7F), supporting the conclusion that aging compromises both mechanotransduction and overall HC performance.

Tissue-specific age-related changes in vestibular and cochlear HCs

The cochlea and vestibule display a different pace of aging, leading to a differential onset and progression of ARHL and ARVD. However, the cellular and molecular processes underlying this difference remain poorly understood (*9*, *65*). We measured auditory brainstem response (ABR), distortion product otoacoustic emissions (DPOAE), and endocochlear potential (EP) to investigate auditory functional decline in our animal cohorts in addition to VsEP (fig. S5A-C). In line with previous studies, we observed a significant elevation in ABR and DPOAE thresholds during aging (*66*). Although some studies from gerbils have reported an age-related decline in EP, our findings revealed no changes in EP in mice. Next, we assessed the age-related morphological changes in the cochlea. The cochlea contains inner and outer HCs (IHCs and OHCs), which are organized tonotopically along the length of the cochlea. Previous findings indicate that the apical and basal turns of the cochlea, which are responsible for detecting low and high frequencies, respectively, show greater vulnerability to aging (*33*, *67*). We observed a significant HC loss, especially in the apical and basal ends of the cochlea (fig. S5D). We also noted age-related hypertrophy and atrophy in the cochlear HCs. In particular, we observed atrophy of both IHCs and OHCs in the apical turn, and OHC atrophy and IHC hypertrophy in the basal turn (fig. S5E).

Next, we assessed age-associated tissue-specific changes between vestibular and cochlear HCs at the molecular level. We conducted a GO analysis to examine the biological processes downregulated in old cochlear HCs compared to age-matched vestibular HCs. We noted a significant downregulation of HC-specific functions, including sensory perception and response, stereocilia-related processes, and synapses in cochlear HCs. We also observed the downregulation of universal processes such as oxidative stress, DNA damage, inflammatory response, and diminished proteostasis and autophagy compared to age-matched old vestibular HCs (Fig.8A and fig. S6). Concordant with that, we observed the age-related downregulation of key genes essential for HC function in old cochlear HCs (Fig.8B). Comparison of age-related log2 fold changes in HC-related gene expression in cochlear and vestibular HCs revealed more pronounced downregulation in cochlear HCs compared to vestibular HCs (Fig.8C). Accumulation of various degenerative molecular changes with aging trigger cellular senescence. It is typically characterized by increased senescence-associated-β-galactosidase (SA-β-gal) activity at pH 6.0 (distinguishing from general β-gal at pH 4.0), allowing selective staining of senescent cells by cleaving X-gal (5-bromo-4-chloro-3-indolyl-β-D-galactopyranoside), resulting in a blue precipitate (*68*, *69*). A previous study shows increased SASP and SA-β-gal activity in the cochlear HCs upon hydrogen peroxide (H_2O_2)-induced DNA damage in an accelerated aging mouse model (*70*). Thus, we assessed SA-β-gal activity in the cochlear and vestibular HCs, and we observed an increase in SA-β-gal activity in both old cochlear and vestibular HCs (Fig.8D). Unlike young vestibular HCs, we also noted the expression of SA-β-gal in young cochlear HCs, indicating potential early onset of age-related molecular changes in cochlear HCs. These findings highlight subtle tissue-specific differences in the aging processes between vestibular and cochlear HCs.

Aging signatures in human vestibular HCs

Previous studies have reported various degenerative changes in vestibular HCs in elderly individuals with ARVD (fig. S7A) (*71*). The age-related changes of the vestibular end organs begin around the age of 55, and more drastic deterioration, including HC loss, occurs after 70-80 years in humans (*9*). However, the molecular changes may occur earlier than the functional and structural changes, gradually accumulating damage and compromising HC integrity. Understanding the age-related molecular changes of the human vestibular HCs remains a significant challenge due to the limited availability of human samples. To examine

the aging signatures in human vestibular HCs, we utilized two publicly available transcriptomic data sets from human organ donors (GSE213796) (GSE207817) (*72*, *73*).

We analyzed vestibular HC datasets from 9.2 fetal weeks and 45-year-old donors for comparison. Our analysis focused on universal hallmarks, as developmental specializations of HCs may still be ongoing at the age of 9.2 fetal weeks. Moreover, 45-year-old datasets were acquired by single-cell RNA sequencing, whereas the fetal data were acquired by single-nucleus RNA sequencing, which excludes cytoplasmic transcripts such as mitochondrial genes. Consequently, we excluded some pathways, such as oxidative stress, from the analysis due to the differences in transcriptomic data acquisition methods. Data were pre-processed and clustered using standard transcriptomic analysis pipeline, and HC clusters were identified using known marker genes (fig. S8). Raw count data from the HCs were extracted and aggregated by averaging counts to generate a pseudobulk data frame containing summed expression values. These values were then scaled and log2-normalized to assess the age-related changes (fig. S7). We observed a reduction in expression of genes linked to global heterochromatin and nucleosome remodeling, changes in histone marks, global DNA hypomethylation, and CpG hypermethylation, indicating epigenetic alterations. Additionally, we noted a substantial downregulation of genes related to DNA damage repair mechanisms, ECM, and intercellular communication. While key genes related to autophagy initiation and progression were enriched, some key genes involved in autophagosome formation were downregulated.

Discussion

Despite the high prevalence of ARVD, its molecular basis remains inadequately understood, hindering the development of targeted treatments (*5*, *9*). In this study, we conducted a comprehensive transcriptomic analysis alongside functional and morphological assessments to examine age-related alterations in the vestibular end organs in mice. We identified genes and molecular processes associated with both universal and cell type-specific aging signatures in the vestibular HCs. Additionally, we uncovered tissue-specific molecular differences in aging between cochlear and vestibular HCs, providing insights into differences in age-related processes within these two mechanosensory systems.

Aging cells, including post-mitotic neurons, photoreceptor cells, and cochlear HCs, exhibit universal aging hallmarks (*33*, *46*, *74*), and we demonstrated that vestibular HCs also conform to these hallmarks. Our data indicated an increase in senescence, marked by a decrease in cyclin-dependent kinases (CDKs), and an increase in cyclin-dependent kinase inhibitors (CDKis) alongside alterations in SASP genes related to laminins, heterochromatic foci, apoptosis, hypoxia, and angiogenesis in old HCs (Fig.4). This was further evident by elevated SA-β-gal staining in old vestibular HCs (Fig.8). Oxidative stress and inflammation play a critical role in ARHL (*75*). Similarly, we observed signatures of increased oxidative stress and low-grade inflammation in old vestibular HCs. Mitochondrial electron transport chain (ETC) byproducts are a major contributor to ROS generation. We detected an age-related increase in the expression of multiple ETC genes, accompanied by elevated expression of antioxidant genes, suggesting increased ROS production along with compensatory clearance. However, we noted that genes related to H_2O_2 free radical clearance were downregulated, suggesting partial ROS clearance. Additionally, genes involved in mitochondrial stress response and quality control were upregulated, further supporting the presence of increased oxidative stress and the activation of adaptive protective mechanisms. While our findings suggested active maintenance of autophagy, decreased expression of several genes involved in autophagosome formation and energy sensing indicate signs of impaired autophagy.

We observed an age-related decrease in genes involved in DNA repair mechanisms, indicating diminished DNA damage repair efficiency in old vestibular HCs in mice and humans. Moreover, we noted significant epigenetic alterations with aging, including alterations in histone marks, DNA methylation, global heterochromatin, and nucleosome remodeling. We also noted a significant reduction in genes involved in ECM, intercellular adhesion, and communication, including cadherins, protocadherins, and integrins, in the old vestibular HCs. Age-related downregulation of these genes may contribute to the degeneration of tip/lateral links, leading to stereocilia and kinocilia fusion (Fig.2). These genes also play a crucial role in cell adhesion, and reduction may lead to an age-related decrease in cell-cell adhesion. Prior studies show a correlation between neurodegenerative diseases and ARHL and ARVD (*57*). Dysregulated proteostasis plays a crucial role in the accumulation of harmful protein aggregates, leading to neurodegenerative diseases (*62*). Overexpression of β-Amyloid and tau proteins in cochlear HCs of Alzheimer's mouse model indicated severe hearing defects and significant HC loss with aging (*76*). Interestingly, we observed the enrichment of neurodegenerative pathways and increased expression of neurodegenerative susceptibility genes, including

Mapt (encodes for tau) and *App* (encodes for amyloid-β precursor protein), in old vestibular HCs (Fig.6), suggesting shared aging patterns between neurons and vestibular HCs.

Due to the multifaceted decline of oculomotor, postural, perceptual, and cognitive functions in ARVD, age-related synaptic and neuronal loss has been considered a contributor to ARVD. While there are mixed findings on age-related synaptic and vestibular ganglion neuron density, recent reports have shown no significant loss of synapses (*3*) and vestibular neurons (*77*). Our findings indicated no substantial changes in genes related to key Ca^{2+} and K^{+} channels (fig. S3). Strikingly, the most prominent age-related changes were observed in the genes associated with the hair bundles and mechanotransduction apparatus (Fig. 5 to 7), which is highly consistent with the age-related stereociliopathy and kinocilia degeneration observed at the morphological level (Fig.2). Interestingly, most of the down-regulated genes, including *Ush1c, Tmc1, Pou4f3, Espn, Fbxo2, Atp2b2, Slc17a8, Homer2, Ccdc39, Ccdc40,* and *Tekt2*, are associated with congenital hearing and balance disorders (*49–51, 55*). Based on the wear and tear theory of aging (*78*), hair bundles are particularly vulnerable to aging as they are the first in line to respond to mechanical stimuli, causing constant mechanoexposure. Since no significant vestibular HC loss was observed at 24 months (Fig.1), the age-related vestibular functional decline may not result from HC loss, but rather from degeneration of the hair bundle structure and mechanotransduction machinery, leading to ARVD (Fig. 7).

Numerous studies have shown diverse molecular changes in various sensory organs during biological aging. These changes vary based on the inherent differences in cellular dynamics in each organ, which regulate the degree and pace of aging (*47, 48*). Examination of the aging signatures of old cochlear HCs relative to age-matched vestibular HCs indicated significant downregulation of processes and genes related to cell type-specific (stereocilia, mechanotransduction) and universal programs (Fig. 8 and fig. S6), aligning with bundle degeneration, cellular hypertrophy/atrophy, and increased loss of cochlear HCs (fig. S5) (*33*). We also noted an early onset of cellular senescence in cochlear HCs compared to vestibular HCs, as evidenced by SA-β-gal activity in young cochlear HCs (Fig.8). This indicates a relatively early onset of aging in cochlear HCs compared to vestibular HCs. However, it remains unclear whether these differences reflect distinct molecular underpinnings. The divergence in aging onset may be influenced by multiple factors, including extrinsic influences (e.g., noise exposure, ototoxic drugs, lifestyle, and systemic health conditions) and intrinsic factors (e.g., genetic predisposition). Moreover, it is also unclear whether the limited capability of vestibular supporting cells to HC conversion may also influence this process.

This study has some limitations. Our findings warrant further investigation, testing mechanistic hypotheses, and using genetic knockout models to examine how these genes impact vestibular function. We assessed the age-related changes in HCs by pooling the HCs from the three vestibular end organs together, which may mask important regional differences in age-related molecular changes. Although we attempted to characterize aging signatures in the human vestibular HCs, these analyses require validation across appropriate age groups to capture both cell type-specific and universal aging signatures. While our findings provide some insights into differences in age-related changes in cochlear and vestibular HCs, it remains challenging to pinpoint a single principle mechanism underlying the difference in the pace of aging between vestibular and auditory organs.

To the best of our knowledge, this is the first study to comprehensively characterize both universal and cell type-specific aging signatures of the vestibular HCs, providing insights into previously unrecognized aspects of vestibular aging. Both universal and cell type-specific aging processes at the molecular level may begin early, leading to the gradual disruption of function, loss of homeostasis, and degenerative changes in vestibular HCs preceding the functional and morphological decline observed at later stages. While our study highlights bundle degeneration and the associated decline in mechanotransduction as a key contributor, it also provides a comprehensive understanding of the underlying mechanisms and molecular drivers of ARVD, paving the way to develop targeted treatment strategies to mitigate ARVD.

Methods

Experimental animals

Wild-type male and female CBA/J mice used in this study were purchased from the Jackson Laboratory (Stock #:000656) and were bred and aged in the Animal Facility of Creighton University under standard conditions. The acoustic environment of the animals was examined by a sound level meter (CEL-500, Casella Cel, UK). The sound levels were 68 dB SPL over 98% of the time, and 75 dB SPL 1-2% of the time. All experimental procedures were approved by the Institutional Animal Care and Use Committee of Creighton University.

Vestibular Sensory Evoked Potential (VsEP)

Animal preparation and VsEP testing were performed as previously described (*79*). Briefly, mice were anesthetized with a combination of Ketamine (126 mg/kg)/Xylazine (14 mg/kg) injected intraperitoneally and supplemented as needed to maintain the anesthesia. Body temperature was maintained at 37±1ºC via a homeothermic heating blanket. The recording electrodes were placed–anterior to the nuchal crest (non-inverting), behind the pinna (inverting), and over the hip (ground) subcutaneously. A custom head clip was used to secure the head to the mechanical shaker (ET-132 Labworks Inc.). The head translation was induced along the naso-occipital axis at a rate of 17 linear pulses per second with alternating polarity and stimulus intensities ranging from +6 to -18 dB relative to 1.0 g/ms (1.0 g = 9.8 m/s^2) adjusted in 3 dB intervals. A broad-band forward masker (50-50,000 Hz, 92 dB SPL) was presented to avoid auditory responses. 128 responses from each of the two polarities (upward and downward head translations) were averaged to yield the mean VsEP responses. First positive (p1) and negative (n1) response peaks correspond to the compound action potential from the vestibular nerve. Thus, the amplitude and latency of these peaks were quantified. The threshold was defined as the mid-level of the lowest stimulus intensity that elicited a detectable response and the next lowest level that did not produce a detectable response.

Auditory brainstem response (ABR) and Distortion Product otoacoustic emissions (DPOAE)

ABRs were recorded from young and old mice in a soundproof chamber as previously described (*33*). The mice were anesthetized with a mixture of ketamine/xylazine, and the body temperature was maintained using a heating pad as mentioned in the VsEP procedure. Platinum recording electrodes were placed at the vertex (non-inverting), mastoid prominence (inverting), and leg (ground) subcutaneously. Tone bursts ranging from 4-50 kHz were used as the stimuli, and ABRs were amplified (100,000x), filtered, and recorded by the TDT RZ6 (Tucker-Davis Technologies, Alachua, FL). 200 stimulus repetitions were used to yield the averaged responses. The lowest sound pressure level (dB) at which any wave (wave I to IV) was visibly detected and reproducible above the noise level was regarded as the ABR threshold. The DPOAE at 2f1-2f2 was recorded in response to f1 and f2, with f1/f2=1.2 and the f2 level was set 10 dB lower than f1. The sound signal was recorded from the inner ear canal via a microphone, amplified, and the fast Fourier transforms were computed from the averaged waveforms obtained from the inner ear sound signal. The f1 sound pressure required to produce a response above the noise level at the frequency of 2f1-f2 was considered the DPOAE threshold. Recorded ABR and DPOAE thresholds were graphed and statistically analyzed using GraphPad Prism.

Endolymphatic potential (ELP) and endocochlear potential (EP)

ELP and EP measurements from the young and old mice were performed as described previously *(27)*. Post anesthesia, tracheotomy was performed in the ventral position without providing artificial respiration. Tissue and musculature overlying the tympanic bulla were removed, and the bulla was opened to access the cochlea. A fine drill was used to make small holes in the lateral wall in the apical and the basal turns of the cochlea. A glass capillary microelectrode (5-8 MΩ) filled with 150 mM KCl was mounted on the Leica micromanipulator. A stable positive DC potential was observed when microelectrode entered the scala media. The responses were amplified (high-pass filter at 1 kHz) using an Axopatch 200B amplifier (Molecular Probe, Sunnyvale, CA, USA) under current-clamp mode and acquired by software pClamp 10 running on an IBM-compatible computer with 16-bit A/D converter (Digidata 1440A). The voltage changes during the penetration were recorded under the gap-free mode via Clampex in the pClamp software (version 10, Molecular Devices) with a sampling frequency of 1 kHz. ELP in the utricle was recorded by inserting the microelectrode through the round window, advancing across scala media, and scala vestibuli to the utricle. The tip of the microelectrode was loaded with fluorescent phalloidin (Invitrogen #565227) diluted in 150 mM KCl (1:100) and injected into the utricle to confirm that the recording was made from the utricle. Post-recording utricle was processed and observed under a confocal microscope.

Recording of vestibular microphonic from utricle maculae

The vestibular microphonic was recorded as described previously (*64*). Vestibular microphonic from the macula of utricle was evoked by driving the inner ear fluid (ref). The stimulus was a 390 Hz sinusoid with a duration of 300 ms and a rise-time of 1 ms from a Burleigh PZ-150M Driver. The piezo actuator was attached to the stapes foot through a tapered glass rod (1.5 cm in length and 0.8 mm in diameter at the stapes foot) after the ossicular chain was severed. The peak-to-peak magnitude of the piezo motion was preset at 3 µm, sufficient to drive a saturated response. We did not expect the contribution of cochlear microphonic to our recording, as the frequency range of the basilar membrane response of CBA/J is above 2 kHz. To rule out the possibility of contribution by cochlear microphonic, the helicotrema in the apical turn of the cochlea was destroyed before the vestibular microphonic was recorded. The microphonic signal from the microelectrode was amplified and high-pass filtered (at 1 kHz) under current-clamp mode using an Axopatch 200B amplifier and acquired by software pClamp 10 running on an IBM-compatible computer with a 16-bit A/D converter (Digidata 1440A). The sampling frequency was 10 kHz. Response from 20 presentations was averaged for each recording.

Scanning electron microscopy (SEM)

Utricle and cristae from the two age groups were dissected and fixed in 2% glutaraldehyde, and 4% PFA in 0.1M sodium cacodylate buffer (pH 7.4) overnight. The fixed samples were washed with 0.1 M phosphate buffer. After removing the otolithic membrane from the utricle, the samples were treated with 1% Osmium tetroxide and washed with 0.1M sodium cacodylate buffer. The samples were then dehydrated using a series of ethanol, followed by critical point drying using carbon dioxide via critical point dryer (EMS 850) and mounted onto the SEM stubs. The morphology of the stereocilia bundle was visualized, and the images were acquired via FEI Quanta 200 scanning electron microscope (ThermoFisher, Hillsboro, OR).

Cell dissociation, cDNA library preparation, and single-cell RNA sequencing

Male and female mice aged 2.5 months (young) and 22 months (old) were used for scRNA-seq. Whole cochlear and vestibular organs were microdissected from the inner ears of CBA/J mice in petri dishes containing cold L-15 media (Gibco #11320033). The sensory epithelia were subjected to enzymatic digestion by transferring them into 1.5 ml eppendorf tubes containing 1 ml/mg collagenase IV (Sigma) in L-15 medium for 10 minutes at room temperature. Then the cells were resuspended in 400 µL of enzyme-free DMEM containing 10% fetal bovine serum. Single-cell suspensions were obtained by trituration using a trimmed 200 µl pipette tip and filtered with a 40 µM strainer. The cells were pelleted by centrifuging at 300 xg for 5 mins at 4°C, then resuspended in media and subsequently quantified the number of cells. 7-8 mice were used for each biological replicate, and 5 biological replicates were obtained for the cochlea and vestibule for the two age groups, respectively. Single-cell capture, and library preparation were performed using droplet-based microfluidic technology, following the manufacturer's instructions for the Chromium Next GEM Single Cell 3′ v3.1 dual index kit. The quality of the obtained libraries was assessed via high-sensitivity DNA kits (Agilent Technologies) using Agilent 4200 TapeStation prior to sequencing with Illumina NovaSeq 6000, acquiring 50,000 reads per cell.

Raw data processing and quality control

Standard 10x Genomics CellRanger pipeline (version 6.1.2) was used for demultiplexing, alignment (10x mouse reference genome mm10), barcode processing, and UMI counting to obtain the filtered count matrices. Processing and visualization of the scRNA-seq data from cochlea and vestibule were performed in R (version 4.2.3). Ten filtered count matrices obtained from 10 biological replicates (5 per age group) from cochlear and vestibular samples were loaded into R, converted to Seurat Objects, and pre-processed to eliminate the poor-quality cells using parameters such as counts, features, percentage of mitochondria, ribosomes, and blood gene content. Cells with at least 200 features, 1000 UMI counts, and less than 25% mitochondrial genes were included for the downstream analysis. Individual Seurat Objects were integrated into a single Seurat Object for each age group, resulting in two main Seurat Objects for young and old samples in both cochlea and vestibule, respectively, creating four Seurat Objects in total.

Normalization, scaling, integration, dimensional reduction, and cluster annotation

Integrated objects were then normalized using log-normalization and scaled using the 'NormalizeData' and 'ScaleData' functions, followed by unsupervised principal component analysis (PCA) and dimensional

reduction. The first 30 PCs were used for the dimensional reduction. The 'FindNeighbors' was used to calculate pairwise similarities and the 'FindClusters' function, which uses the Louvain algorithm, was applied with the optimal cluster resolution for all four Seurat Objects, respectively. The top markers of each cluster were identified using the 'Findmarkers' function. Samples were then visualized via uniform manifold approximation and projection (UMAP). This dimensional reduction method uses k-nearest neighbors and Euclidean distance algorithms, preserving the local and global structure of the data. A total of 33 and 27 distinct clusters were identified from the initial clustering of young and old vestibular samples, while 31 and 33 clusters were identified from young and old cochlear samples, respectively. Previously reported cell-type-specific pan markers were used to classify the cell-type distribution in young and old vestibular and cochlear samples. Based on the known marker genes, we identified many cell types, including vestibular type I and II HCs as well as cochlear IHCs and OHCs. Vestibular and cochlear HC clusters from the two age groups were then subsetted out and reclustered for the downstream analysis to investigate age-related molecular changes.

Pseudobulk gene expression analysis

Subsetted out young and old type I and II HCs were used to extract raw count data from single cells and aggregated them by averaging counts across young and old biological replicates to generate a pseudobulk data frame that contains summed expression values for the 4 HC groups (young and old type I and II). Expression values were then scaled and log2-normalized (table S2). Genes associated with universal aging pathways were gathered manually from multiple publicly available resources such as Aging Atlas, GenAge, SASP Atlas, and literature. Then, the general trends in the age-related expression changes were evaluated using genes associated with each aging pathway using the 'ComplexHeatMap' function. Expression data were extracted and centered using Cluster 3.0 (version 1.59), and heatmaps were generated using JAVA TreeView (version 1.2.1). For human vestibular HC analysis, the data sets were obtained from the GEO, pre-processed, and annotated the clusters following the same pipeline used for the murine pseudobulk analysis.

Differentially expressed gene (DEG) analysis

Principle component analysis (PCA) was performed to assess the variance among young and old vestibular datasets by using the 'DESeq2' package in Seurat. The default statistical test in the 'DESeq2' package is the Wald test with Benjamini-Hochberg correction for multiple testing. DESeq2 uses a generalized linear model (GLM) to identify DEGs within multiple groups, and variance stabilizing transformation (VST) is used to assess the variance, revealing the biological patterns in data. DESeq2 pseudo bulk differential expression pipeline was used to generate Venn diagram via ggplot2 based 'ggVennDiagram' package. The Wilcoxon rank-sum test with Bonferroni correction in Seurat was used to assess the differentially expressed genes in young and old samples and subsequently visualized as heatmaps and volcano plots. The top 50 DEGs were identified using the 'FindMarkers' function, using young HCs as the reference and old HCs as the test group to generate heatmaps using the 'DoHeatmap' function. The genes at least expressed in 25% of cells in the cluster were considered for this analysis and ordered according to Log2 fold change (Log2FC). The 'EnhancedVolcano' function was used to generate the volcano plots using a fold-change cut-off (FCcutoff) value of 0.25 and a p-value (pCutoff) of 0.05.

Functional enrichment analysis

The biological relevance of the top DEGs in the old samples compared to the young samples was assessed using gene ontology (GO) enrichment and over-representation analysis. EnrichGO in the 'clusterProfiler' package in Seurat was used to conduct this analysis. This algorithm uses the Hypergeometric test with the Benjamini-Hochberg method for multiple testing corrections. The top genes that were downregulated with aging (Log2FC<0) were used to assess the biological processes (BP), and molecular function (MF). Pairwise semantic similarity was computed for clustering the GO terms, and data were visualized as dot plots, emap plots, and cnet plots. Kyoto Encyclopedia of Genes and Genomes (KEGG) analysis was performed to assess the pathways enriched in old vestibular HCs (Log2FC<0). DESeq2 was used to generate a pseudo bulk data matrix as described above in the DEG analysis. The 'enrichKEGG' function in the 'clusterProfiler' package was used for this analysis. This algorithm also uses the Hypergeometric test with the Benjamini-Hochberg adjustment.

Histology

Temporal bones were isolated from the young, and old mice, and a hole was made in the apical cochlea followed by overnight fixation with 4% PFA (Electron Microscopy Science, Cat: 15710) in PBS (Cytvia, SH30258.02). Tissues were thoroughly washed with 1x PBS, cleared with xylene, and rehydrated with a series of ethanol. Then tissues were embedded in paraffin wax, and the 8-10 µm thick sections were made using a microtome. H&E staining was performed using Fisher Scientific Gemini^{TM} AS automated slide stainer. The slides were loaded onto the Gemini AS basket and immersed in xylene for 3 minutes (x3), followed by a series of ethanol washes (100%, 95%, and 70%), 2 mins each. Next, the slides were immersed in hematoxylin for 2 mins, rinsed with water, and clarifier two was added (20 seconds) followed by 1 min rinse with water. Bluing reagent was added for 1 min, followed by 1 min water rinse. Slides were then submerged in 70% and 95% ethanol (2 mins each). Then the slides were immersed with counterstain eosin for 1 min and the slides were then immersed in 100% ethanol (2 mins X3) followed by incubation with xylene (2 mins x3) and mounting. Images were taken using Olympus VS120 virtual slide scanner.

Immunostaining and Confocal imaging

Temporal bones were isolated from the young, and old mice, and a hole was made in the apical cochlea followed by overnight fixation with 4% PFA (Electron Microscopy Science, Cat: 15710) in PBS (Cytvia, SH30258.02) solution at 4°C. For the whole mount preparations, the vestibule and cochlea were microdissected from the temporal bones, then permeabilized in 1x PBST (0.3% Triton-X-100 in PBS) for 30 min followed by blocking with 10% normal goat serum (Sera care, Cat: 5560-0007) for 1h at room temperature. Tissues were incubated with primary antibodies overnight at 4°C on a rocker. The samples were thoroughly washed with 1x PBST for 30 min and incubated for 40 min at room temperature with secondary antibodies and counterstains such as DAPI and Phalloidin. The tissues were subsequently washed with 1x PBST for 40 min and carefully mounted with Fluoromount mounting media. For cryosections, the tissues were fixed overnight with 4% PFA in PBS solution at 4°C and decalcified in 10% EDTA (E671001-0500; Sangon Biotech). Tissues were washed with PBS post-fixing and cryoprotected in a sucrose gradient of 15% and 30%. The sections were then embedded in OCT (Fisher Healthcare, Cat: 4585) and kept on dry ice. 10 µm thick sections were made using Cryostat (Leica CM 1950). We used primary antibodies to immunolabel the following markers: anti-ESPN, anti-CCDC39, anti-CCDC40, anti-MYO6, anti-MYO7A, anti-acetylated-β-Tubulin, anti-SOX2, Phalloidin Flour^{TM} 488, Phalloidin Flour^{TM} Plus 405. Goat anti-rabbit Fluor 568, donkey anti-mouse 568, goat anti-rabbit Fluor 488, goat anti-mouse Fluor 488 secondary antibodies were used (table S1). Confocal images were taken via Zeiss LSM 700 upright microscope, Zeiss LSM 700 inverted microscope, and Zeiss LSM 980 inverted confocal microscope. Optical image sections were captured using orthoslicer of Imaris application, and Adobe Photoshop was used to remove the background and isolate individual hair cell images.

RNAscope *in situ* hybridization

Decalcification and microdissection of young and old vestibular and cochlear tissues were performed as described above in the immunohistochemistry. Gene expression validations were performed using RNAscope *in situ* hybridization following the manufacturer's instructions for RNAscope^{TM} 2.5 HD Red Assay from Advanced Cell Diagnostics (ACD Bio, Cat: 322360). In brief, paraffin-embedded tissue sections of 10 µm were baked in the HybEZ oven at 60°C followed by 10 mins incubation with xylene and ethanol to dewax and dehydrate, respectively. Sections were then subjected to hydrogen peroxide and protease treatment before incubation with probes for 2h at 40°C. Subsequently, amplification, detection, and counterstaining with DAPI were carried out before the samples were mounted. Images were acquired via Zeiss 700 inverted confocal microscope, and the obtained z-stacks were presented in maximum-intensity projection. Following this procedure, 10 probes were used to assess the gene expression, including *Espn*, *Tmc1*, *Atp2b2*, Fbxo2, *Pou4f3*, *Homer2*, *Gjb2*, *Hspb1*, and *DapB* (negative control). The quantification of RNAscope puncta density was performed using FIJI, and the statistical analyses were performed using GraphPad Prism.

FM1-43FX (*N*-(3-Triethylammoniumpropyl)-4-(4-(Dibutylamino) Styryl) Pyridinium Dibromide) dye uptake assay

As described previously (*63*), the inner ears were harvested from the young and old mice and transferred to DMEM supplemented with 10% FBS, and the utricle and cristae were microdissected efficiently. The tissues were immersed in 10 µM FM1-43 (Invitrogen, Cat: F35355) for 1 min 30 seconds, followed by washes with DMEM. The tissues were fixed with 4% PFA for 20 minutes, washed with DMEM, and mounted. The images

were acquired using Zeiss 980 confocal microscope. Images were processed using FIJI, and optical sections were made using Orthoslicer in Imaris. Fluorescence intensities were quantified using FIJI, and statistical analysis was performed using GraphPad Prism.

Senescence-associated β-galactosidase (SA-β-gal) staining and imaging

According to the user manual, senescence-associated β-gal (SA-β-gal) staining was performed using senescence-associated β-gal (Cell Signaling #9860) staining kit. The temporal bones were fixed in the 1X fixative solution provided in the kit for 30 minutes, as previously described (*70*). Then the cochlea and the vestibular system were microdissected. According to the manufacturer's protocol, 1x staining solution, X-Gal, and β-galactosidase staining solutions were prepared. The cochlear and vestibular whole mounts were incubated in the staining solution overnight at 37°C. Samples were mounted and imaged using Olympus VS120 virtual slide scanner.

References

1. C. López-Otín, M. A. Blasco, L. Partridge, M. Serrano, G. Kroemer, The hallmarks of aging. *Cell* **153**, 1194 (2013).
2. C. López-Otín, M. A. Blasco, L. Partridge, M. Serrano, G. Kroemer, Hallmarks of aging: An expanding universe. *Cell* **186**, 243–278 (2023).
3. V. G. Paplou, N. M. A. Schubert, M. van Tuinen, S. Vijayakumar, S. J. Pyott, Functional, Morphological and Molecular Changes Reveal the Mechanisms Associated with Age-Related Vestibular Loss. *Biomolecules* **13** (2023).
4. M. R. Bowl, S. J. Dawson, Age-related hearing loss. *Cold Spring Harb Perspect Med* **9** (2019).
5. C. K. Zalewski, Aging of the Human Vestibular System. *Semin Hear* **36**, 175–196 (2015).
6. U. Rosenhall, W. Rubin, Degenerative changes in the human vestibular sensory epithelia. *Acta Otolaryngol* **79**, 67–80 (1975).
7. L. Ji, S. Zhai, Aging and the peripheral vestibular system. *J Otol* **13**, 138–140 (2018).
8. H. F. Schuknecht, Presbycusis. *Laryngoscope* **65**, 402–419 (1955).
9. V. Paplou, N. M. A. Schubert, S. J. Pyott, Age-Related Changes in the Cochlea and Vestibule: Shared Patterns and Processes. *Front Neurosci* **15** (2021).
10. D. Allen, L. Ribeiro, Q. Arshad, B. M. Seemungal, Age-Related Vestibular Loss: Current Understanding and Future Research Directions. *Front Neurol* **7**, 231 (2016).
11. S. Iwasaki, T. Yamasoba, Dizziness and Imbalance in the Elderly: Age-related Decline in the Vestibular System. *Aging Dis* **6**, 38 (2014).
12. M. Fetter, Vestibular System Disorders. *Encyclopedia of Life Sciences*, doi: 10.1002/9780470015902.A0002213.PUB2 (2010).
13. P. G. Gillespie, U. Müller, Mechanotransduction by Hair Cells: Models, Molecules, and Mechanisms. *Cell* **139**, 33 (2009).
14. H. H. Lindeman, Regional Differences in Structure of the Vestibular Sensory Regions. *J Laryngol Otol* **83**, 1–17 (1969).
15. R. A. EATOCK, M. J. HUTZLER, Ionic Currents of Mammalian Vestibular Hair Cellsa. *Ann N Y Acad Sci* **656**, 58–74 (1992).
16. S. N. Merchant, K. Tsuji, C. Wall, L. Velázquez-Villaseñor, R. J. Glynn, S. D. Rauch, Temporal bone studies of the human peripheral vestibular system. Normative vestibular hair cell data. *Ann Otol Rhinol Laryngol Suppl* **181**, 3–13 (2000).
17. S. Brosel, C. Laub, A. Averdam, A. Bender, M. Elstner, Molecular aging of the mammalian vestibular system. *Ageing Res Rev* **26**, 72–80 (2016).
18. P. D. Sloane, R. W. Baloh, V. Honrubia, The vestibular system in the elderly: Clinical implications. *American Journal of Otolaryngology--Head and Neck Medicine and Surgery* **10**, 422–429 (1989).
19. U. Rosenhall, Degenerative patterns in the aging human vestibular neuro-epithelia. *Acta Otolaryngol* **76**, 208–220 (1973).
20. R. D. Frisina, A. Singh, M. Bak, S. Bozorg, R. Seth, X. Zhu, F1 (CBA×C57) mice show superior hearing in old age relative to their parental strains: Hybrid vigor or a new animal model for "Golden Ears"? *Neurobiol Aging* **32**, 1716–1724 (2011).
21. S. H. Sha, A. Kanicki, G. Dootz, A. E. Talaska, K. Halsey, D. Dolan, R. Altschuler, J. Schacht, Age-related auditory pathology in the CBA/J mouse. *Hear Res* **243**, 87–94 (2008).
22. T. A. Jones, S. M. Jones, S. Vijayakumar, A. Brugeaud, M. Bothwell, C. Chabbert, The adequate stimulus for mammalian linear vestibular evoked potentials (VsEPs). *Hear Res* **280**, 133–140 (2011).
23. B. Mock, T. A. Jones, S. M. Jones, Gravity receptor aging in the CBA/CAJ strain: A comparison to auditory aging. *JARO - Journal of the Association for Research in Otolaryngology* **12**, 173–183 (2011).
24. G. Leng, The Davis theory: A review, and implications of recent electrophysiological evidence. *Hear Res* **3**, 17–25 (1980).
25. C. Köppl, V. Wilms, I. J. Russell, H. G. Nothwang, Evolution of Endolymph Secretion and Endolymphatic Potential Generation in the Vertebrate Inner Ear. *Brain Behav Evol* **92**, 1–31 (2018).

26. P. Wangemann, Comparison of ion transport mechanisms between vestibular dark cells and strial marginal cells. *Hear Res* **90**, 149–157 (1995).
27. Y. Li, H. Liu, X. Zhao, D. Z. He, Endolymphatic Potential Measured From Developing and Adult Mouse Inner Ear. *Front Cell Neurosci* **14**, 584928 (2020).
28. S. D. Rauch, L. Velazquez-Villaseñor, P. S. Dimitri, S. N. Merchant, Decreasing hair cell counts in aging humans. *Ann N Y Acad Sci* **942**, 220–227 (2001).
29. C. Spoon, W. Grant, Biomechanical measurement of kinocilium. *Methods Enzymol* **525**, 21–43 (2013).
30. J. Lu, L. Hu, B. Ye, H. Hu, Y. Tao, Y. Shu, Hao Chiang, V. Borse, M. Xiang, H. Wu, A. S. B. Edge, F. Shi, Increased Type I and Decreased Type II Hair Cells after Deletion of Sox2 in the Developing Mouse Utricle. *Neuroscience* **422**, 146–160 (2019).
31. J. S. Stone, R. Pujol, T. B. Nguyen, B. C. Cox, The transcription factor sox2 is required to maintain the cell type-specific properties and innervation of type II vestibular hair cells in adult mice. *Journal of Neuroscience* **41**, 6217–6233 (2021).
32. B. Boëda, D. Weil, C. Petit, A specific promoter of the sensory cells of the inner ear defined by transgenesis. *Hum Mol Genet* **10**, 1581–1589 (2001).
33. H. Liu, K. P. Giffen, L. Chen, H. J. Henderson, T. A. Cao, G. A. Kozeny, K. W. Beisel, Y. Li, D. Z. He, Molecular and cytological profiling of biological aging of mouse cochlear inner and outer hair cells. *Cell Rep* **39** (2022).
34. C. E. Finch, Neuron atrophy during aging: programmed or sporadic? *Trends Neurosci* **16**, 104–110 (1993).
35. Z. Xu, A. Tavakoli, S. Kulasooriya, H. Liu, S. Tu, C. Bloom, Y. Li, T. D. Johnson, J. Zuo, L. Tao, B. Kachar, D. Z. He, The Dual Molecular Identity of Vestibular Kinocilia: Bridging Structural and Functional Traits of Primary and Motile Cilia. *bioRxiv*, doi: 10.1101/2025.04.16.647417 (2025).
36. B. Kachar, M. Parakkal, J. Fex, Structural basis for mechanical transduction in the frog vestibular sensory apparatus: I. The otolithic membrane. *Hear Res* **45**, 179–190 (1990).
37. S. Brosel, C. Laub, A. Averdam, A. Bender, M. Elstner, Molecular aging of the mammalian vestibular system. *Ageing Res Rev* **26**, 72–80 (2016).
38. M. D. Luecken, F. J. Theis, Current best practices in single-cell RNA-seq analysis: a tutorial. *Mol Syst Biol* **15** (2019).
39. S. McInturff, J. C. Burns, M. W. Kelley, Characterization of spatial and temporal development of Type I and Type II hair cells in the mouse utricle using new cell-type-specific markers. *Biol Open* **7** (2018).
40. J. C. Burns, M. C. Kelly, M. Hoa, R. J. Morell, M. W. Kelley, Single-cell RNA-Seq resolves cellular complexity in sensory organs from the neonatal inner ear. *Nature Communications 2015 6:1* **6**, 1–16 (2015).
41. J. Campisi, J. K. Andersen, P. Kapahi, S. Melov, Cellular senescence: A link between cancer and age-related degenerative disease? *Semin Cancer Biol* **21**, 354–359 (2011).
42. J. H. Lee, E. W. Kim, D. L. Croteau, V. A. Bohr, Heterochromatin: an epigenetic point of view in aging. *Exp Mol Med* **52**, 1466–1474 (2020).
43. T. Schmauck-Medina, A. Molière, S. Lautrup, J. Zhang, S. Chlopicki, H. B. Madsen, S. Cao, C. Soendenbroe, E. Mansell, M. B. Vestergaard, Z. Li, Y. Shiloh, P. L. Opresko, J. M. Egly, T. Kirkwood, E. Verdin, V. A. Bohr, L. S. Cox, T. Stevnsner, L. J. Rasmussen, E. F. Fang, New hallmarks of ageing: a 2022 Copenhagen ageing meeting summary. *Aging (Albany NY)* **14**, 6829 (2022).
44. S. F. Tadros, M. D'Souza, X. Zhu, R. D. Frisina, Gene expression changes for antioxidants pathways in the mouse cochlea: Relations to age-related hearing deficits. *PLoS One* **9** (2014).
45. K. M. Dodson, S. H. Blanton, K. O. Welch, V. W. Norris, R. L. Nuzzo, J. A. Wegelin, R. S. Marin, W. E. Nance, A. Pandya, K. S. Arnos, Vestibular Dysfunction in DFNB1 deafness. *Am J Med Genet A* **155**, 993 (2011).
46. G. Sun, Y. Zheng, X. Fu, W. Zhang, J. Ren, S. Ma, S. Sun, X. He, Q. Wang, Z. Ji, F. Cheng, K. Yan, Z. Liu, J. C. I. Belmonte, J. Qu, S. Wang, R. Chai, G. H. Liu, Single-cell transcriptomic atlas of mouse cochlear aging. *Protein Cell* **14**, 180–201 (2023).
47. R. Yamamoto, R. Chung, J. M. Vazquez, H. Sheng, P. L. Steinberg, N. M. Ioannidis, P. H. Sudmant, Tissue-specific impacts of aging and genetics on gene expression patterns in humans. *Nat Commun* **13**, 1–12 (2022).
48. K. Jin, Z. Yao, C. T. J. van Velthoven, E. S. Kaplan, K. Glattfelder, S. T. Barlow, G. Boyer, D. Carey, T. Casper, A. B. Chakka, R. Chakrabarty, M. Clark, M. Departee, M. Desierto, A. Gary, J. Gloe, J.

Goldy, N. Guilford, J. Guzman, D. Hirschstein, C. Lee, E. Liang, T. Pham, M. Reding, K. Ronellenfitch, A. Ruiz, J. Sevigny, N. Shapovalova, L. Shulga, J. Sulc, A. Torkelson, H. Tung, B. Levi, S. M. Sunkin, N. Dee, L. Esposito, K. A. Smith, B. Tasic, H. Zeng, Brain-wide cell-type-specific transcriptomic signatures of healthy ageing in mice. *Nature 2025 638:8049* **638**, 182–196 (2025).

49. J. J. Smits, J. Oostrik, A. J. Beynon, S. G. Kant, P. A. M. de Koning Gans, L. J. C. Rotteveel, J. S. Klein Wassink-Ruiter, R. H. Free, S. M. Maas, J. van de Kamp, P. Merkus, W. Koole, I. Feenstra, R. J. C. Admiraal, C. P. Lanting, M. Schraders, H. G. Yntema, R. J. E. Pennings, H. Kremer, De novo and inherited loss-of-function variants of ATP2B2 are associated with rapidly progressive hearing impairment. *Hum Genet* **138**, 61–72 (2019).
50. S. Naz, A. J. Griffith, S. Riazuddin, L. L. Hampton, J. F. Battey, S. N. Khan, S. Riazuddin, E. R. Wilcox, T. B. Friedman, Mutations of ESPN cause autosomal recessive deafness and vestibular dysfunction. *J Med Genet* **41**, 591–595 (2004).
51. B. Pan, C. Askew, A. Galvin, S. Heman-Ackah, Y. Asai, A. A. Indzhykulian, F. M. Jodelka, M. L. Hastings, J. J. Lentz, L. H. Vandenberghe, J. R. Holt, G. S. Géleóc, Gene therapy restores auditory and vestibular function in a mouse model of Usher syndrome type 1c. *Nature Biotechnology 2017 35:3* **35**, 264–272 (2017).
52. J. R. McFadden, C. D. P. Tolete, Y. Huang, E. Macnamara, D. Sept, G. Nesterova, W. A. Gahl, D. L. Sackett, M. C. V. Malicdan, Clinical, genetic, and structural characterization of a novel TUBB4B tubulinopathy. *Mol Genet Metab Rep* **36** (2023).
53. B. J. Perrin, K. J. Sonnemann, J. M. Ervasti, β-Actin and γ-Actin are each dispensable for auditory hair cell development but required for stereocilia maintenance. *PLoS Genet* **6**, 1–12 (2010).
54. Z. Xu, A. Tavakoli, S. Kulasooriya, H. Liu, S. Tu, C. Bloom, Y. Li, J. Zuo, L. Tao, B. Kachar, D. Z. He, Kinocilia of Vestibular Hair Cells: Bridging Molecular and Functional Traits of Primary and Motile Cilia. *bioRxiv*, 2025.04.16.647417 (2025).
55. I. Aprea, A. Wilken, C. Krallmann, T. Nöthe-Menchen, H. Olbrich, N. T. Loges, G. W. Dougherty, D. Bracht, C. Brenker, S. Kliesch, T. Strünker, F. Tüttelmann, J. Raidt, H. Omran, Pathogenic gene variants in CCDC39, CCDC40, RSPH1, RSPH9, HYDIN, and SPEF2 cause defects of sperm flagella composition and male infertility. *Front Genet* **14**, 1117821 (2023).
56. J. Coto, C. L. Alvarez, I. Cejas, B. M. Colbert, B. E. Levin, J. Huppert, T. Rundek, C. Balaban, S. H. Blanton, D. J. Lee, D. Loewenstein, M. Hoffer, X. Z. Liu, Peripheral vestibular system: Age-related vestibular loss and associated deficits. *J Otol* **16**, 258–265 (2021).
57. F. H. Previc, Vestibular loss as a contributor to Alzheimer's disease. *Med Hypotheses* **80**, 360–367 (2013).
58. B. R. Leavitt, H. B. Kordasiewicz, S. A. Schobel, Huntingtin-Lowering Therapies for Huntington Disease: A Review of the Evidence of Potential Benefits and Risks. *JAMA Neurol* **77**, 764–772 (2020).
59. C. S. Leblond, H. M. Kaneb, P. A. Dion, G. A. Rouleau, Dissection of genetic factors associated with amyotrophic lateral sclerosis. *Exp Neurol* **262**, 91–101 (2014).
60. H. Gossye, S. Engelborghs, C. Van Broeckhoven, J. van der Zee, C9orf72 Frontotemporal Dementia and/or Amyotrophic Lateral Sclerosis. *GeneReviews®* (2020).
61. M. Neumann, R. Rademakers, S. Roeber, M. Baker, H. A. Kretzschmar, I. R. A. MacKenzie, A new subtype of frontotemporal lobar degeneration with FUS pathology. *Brain* **132**, 2922 (2009).
62. C. Duran-Aniotz, I. Moreno-Gonzalez, D. B. Medinas, R. Morales, Editorial: Protein Misfolding and Proteostasis Impairment in Aging and Neurodegeneration: From Spreading Studies to Therapeutic Approaches. *Front Aging Neurosci* **13** (2022).
63. J. R. Meyers, R. B. MacDonald, A. Duggan, D. Lenzi, D. G. Standaert, J. T. Corwin, D. P. Corey, Lighting up the Senses: FM1-43 Loading of Sensory Cells through Nonselective Ion Channels. *Journal of Neuroscience* **23**, 4054–4065 (2003).
64. C. J. Pastras, I. S. Curthoys, D. J. Brown, In vivo recording of the vestibular microphonic in mammals. *Hear Res* **354**, 38–47 (2017).
65. M. Arslan, The Senescence of the Vestibular Apparatus. *Pract Otorhinolaryngol (Basel)* **19**, 475–483 (1957).
66. Z. Qin, M. Wood, J. J. Rosowski, Measurement of Conductive Hearing Loss in Mice. *Hear Res* **263**, 93 (2009).
67. S. H. Sha, A. Kanicki, G. Dootz, A. E. Talaska, K. Halsey, D. Dolan, R. Altschuler, J. Schacht, Age-related auditory pathology in the CBA/J mouse. *Hear Res* **243**, 87–94 (2008).

68. Y. Valieva, E. Ivanova, A. Fayzullin, A. Kurkov, A. Igrunkova, Senescence-Associated β-Galactosidase Detection in Pathology. *Diagnostics* **12**, 2309 (2022).
69. D. R. Krishna, B. Sperker, P. Fritz, U. Klotz, Does pH 6 β-galactosidase activity indicate cell senescence? *Mech Ageing Dev* **109**, 113–123 (1999).
70. N. Benkafadar, F. François, C. Affortit, F. Casas, J. C. Ceccato, J. Menardo, F. Venail, B. Malfroy-Camine, J. L. Puel, J. Wang, ROS-Induced Activation of DNA Damage Responses Drives Senescence-Like State in Postmitotic Cochlear Cells: Implication for Hearing Preservation. *Mol Neurobiol* **56**, 5950–5969 (2019).
71. R. R. Taylor, D. J. Jagger, S. R. Saeed, P. Axon, N. Donnelly, J. Tysome, D. Moffatt, R. Irving, P. Monksfield, C. Coulson, S. R. Freeman, S. K. Lloyd, A. Forge, Characterizing human vestibular sensory epithelia for experimental studies: New hair bundles on old tissue and implications for therapeutic interventions in ageing. *Neurobiol Aging* **36**, 2068–2084 (2015).
72. W. H. van der Valk, E. S. A. van Beelen, M. R. Steinhart, C. Nist-Lund, D. Osorio, J. C. M. J. de Groot, L. Sun, P. P. G. van Benthem, K. R. Koehler, H. Locher, A single-cell level comparison of human inner ear organoids with the human cochlea and vestibular organs. *Cell Rep* **42**, 112623 (2023).
73. T. Wang, A. H. Ling, S. E. Billings, D. K. Hosseini, Y. Vaisbuch, G. S. Kim, P. J. Atkinson, Z. N. Sayyid, K. A. Aaron, D. Wagh, N. Pham, M. Scheibinger, R. Zhou, A. Ishiyama, L. S. Moore, P. S. Maria, N. H. Blevins, R. K. Jackler, J. C. Alyono, J. Kveton, D. Navaratnam, S. Heller, I. A. Lopez, N. Grillet, T. A. Jan, A. G. Cheng, Single-cell transcriptomic atlas reveals increased regeneration in diseased human inner ear balance organs. *Nature Communications 2024 15:1* **15**, 1–19 (2024).
74. A. Cvekl, J. Vijg, Aging of the eye: Lessons from cataracts and age-related macular degeneration. *Ageing Res Rev* **99** (2024).
75. C. Fujimoto, T. Yamasoba, Oxidative stresses and mitochondrial dysfunction in age-related hearing loss. *Oxid Med Cell Longev* **2014** (2014).
76. Y. Omata, S. Tharasegaran, Y. M. Lim, Y. Yamasaki, Y. Ishigaki, T. Tatsuno, M. Maruyama, L. Tsuda, Expression of amyloid-β in mouse cochlear hair cells causes an earlyonset auditory defect in high-frequency sound perception. *Aging* **8**, 427–439 (2016).
77. G. Wan, L. Ji, T. Schrepfer, S. Gong, G. P. Wang, G. Corfas, Synaptopathy as a mechanism for age-related vestibular dysfunction in mice. *Front Aging Neurosci* **11** (2019).
78. A. K. Rzadzinska, M. E. Schneider, C. Davies, G. P. Riordan, B. Kachar, An actin molecular treadmill and myosins maintain stereocilia functional architecture and self-renewal. *Journal of Cell Biology* **164**, 887–897 (2004).
79. S. Vijayakumar, F. F. Depreux, F. M. Jodelka, J. J. Lentz, F. Rigo, T. A. Jones, M. L. Hastings, Rescue of peripheral vestibular function in Usher syndrome mice using a splice-switching antisense oligonucleotide. *Hum Mol Genet* **26**, 3482–3494 (2017).

Acknowledgment
We thank Dr. Marisa Zallocchi for generously sharing the reagents. This research partially utilized the Auditory and Vestibular Technology (AVT) core (grants GM103427, GM139762), Histology and Molecular core facility (grants RRID:SCR_025163), Department of Chemistry & Biochemistry (EPSCoR) at Creighton University, and DNA Sequencing Core Facility at the University of Nebraska (grant RR018788).

Funding
This work was supported by the National Institute on Deafness and other Communication Disorders (NIDCD), National Institutes of Health (R01 DC016807) to D.H., National Institute on Deafness and other Communication Disorders (NIDCD), National Institutes of Health (IRP fund Z01-DC000002) to B.K and Dr. Richard. J. Bellucci Pre-doctoral research award to S.K. by Bellucci De Paoli Family Foundation and Creighton University School of Medicine.

Author Contributions
Conceptualization: S.K., D.H.
Methodology: S.K., H.L., D.H.
Investigation: S.K., H.L., D.H., S.V., S.T., C.B., M.Z., B.J.B.
Visualization: S.K.
Supervision: D.H., L.T., B.K.
Writing—original draft: S.K.
Writing—review & editing: S.K., D.H., B.K., L.T., C.B., S.V., B.J.B.

Competing interests
All authors declare no competing interests.

Data and materials availability
Publicly available standard packages and algorithms were used for the analysis of our sequencing data and no custom code or algorithms were generated. All relevant data are included in this paper and the supplementary materials. The single-cell RNA sequencing data generated in this study have been deposited in the NCBI Gene Expression Omnibus (GEO) under the accession numbers GSE283534 (young CBA/J) and GSE283708 (old CBA/J).

Fig. 1. Age-related functional and cellular changes in the vestibular HCs. (**A** to **C).** Measurements of VsEP from the young and old mice (n = 8 per age group). (A) 3 representative wave forms from each age group depicting the reduction in response amplitude, (B) elevation of threshold in the old animals compared to young animals, and (C) quantification of reduction in response amplitude (left) and increase in latency in the old group compared to the young group (right). P1 and N1 indicate the first positive and negative peaks. **(D)** Graphical illustration of measurement of ELP using a glass capillary microelectrode (D), and ELP magnitude quantifications (n=6 per age group). **(E)** Representative images of young and old striolar and extrastriolar sensory epithelia (cropped region) from utricle whole mounts immunolabeled with anti-MYO7A and anti-SOX2, Nuclei were stained with DAPI. Scale bar, 10 µm. **(F)** Quantifications of total HC density (n=4), as well as type I and II HC density in striolar and extrastriolar regions (n=2). **(G)** Representative images of young and old H&E sections indicating type I and II HCs from the saccule and cristae. **(H)** Confocal virtual sectioning images of some individual HCs demonstrating cellular hypertrophy (elongation) and atrophy (shortening) in the three vestibular end organs acquired by the ortho slicer tool in Imaris application. Scale bar, 10 µm. **(I)** Quantification of HC lengths in the three vestibular end organs from histological analysis. Individual cell measurements of type I and II HCs were taken along the sensory epithelia (utricle, saccule, and cristae) from two technical replicates per biological replicate (n=2 per age group). Data are shown as mean ± SEM, *p <0.05, **p <0.01, ****p<0.0001, ns - non-significant by unpaired t-test.

Fig. 2. Age-related changes in the hair bundle. (A) High-resolution confocal microscopic images of young and old utricle and cristae, indicating stereocilia and kinocilia degeneration with aging (a). Stereocilia were stained with Phalloidin, and kinocilia were immunolabeled with anti-acetylated-β-tubulin. Scale bar, 5 µm. Lower right representative images indicate the kinociliary bulb formation (b), fusion (c), looping, and knotting (d) with aging. **(B)** Quantifications of degenerative changes in young and old utricle and cristae (n=4). The total number of bundles and bundles with degenerative signs were quantified from two different areas in striolar and extrastriolar regions per biological replicate in the two age groups and presented as a percentage. Data shown as mean ± SEM. **(C)** Representative SEM images of hair bundles from young and old utricle and cristae indicating signs of degeneration. Scale bar, 5 µm. **(D)** Examples of various signs of bundle degeneration. Scale bar, 5 µm. All images were taken from regions with obvious signs of bundle degeneration.

Fig. 3: Vestibular cell type distribution and HC cluster annotation. (A) An illustration of the experimental workflow of scRNA-sequencing, data analysis, and visualization. **(B and C)** Uniform manifold approximation and projection (UMAP) plot showing the distribution of different cell types in young and old vestibular samples, respectively. This dimensional reduction method uses k-nearest neighbors (KNN) and the Euclidean distance algorithm to construct a low-dimensional graph for visualization. **(D and G)** Dot plots indicating the expression of known marker genes and gene signatures used for cluster annotation. The dot size represents the percentage of cells expressing the genes from each cluster, whereas the color indicates the expression level. Expression levels are normalized via z-score normalization. Thus, the average expression is zero, and positive or negative values indicate expression above or below average. **(E and H)** Feature plots demonstrating the HC-specific pan marker gene expression in the HC clusters identified in the UMAPs. **(F and I)** Number of type I and II HCs identified from young and old vestibular samples for the downstream analysis (n=7-8 mice per biological replicate).

Fig.4. Universal hallmarks of aging in vestibular HCs. (A) Complex heatmaps indicating the enrichment of genes associated with universal hallmarks of aging, including senescence and SASP, loss of proteostasis, oxidative stress, autophagy, inflammaging, DNA damage repair, intercellular communication, and epigenetic alterations in the old vestibular HCs compared to young HCs. Single-cell counts were aggregated. Pseudo-bulk gene expression values were then scaled and log2-transformed. Expression values were centered by Cluster 3.0, and heatmaps were generated using JAVA TreeView. The color scale indicates the expression level. **(B)** RNAscope *in situ* hybridization of *Hspb1* (proteostasis) and *Gjb2* (intercellular communication) in young and old otoliths (n=3) and crista (n=2). Scale bar, 10 µm. The puncta density for each gene was quantified using FIJI. Data shown as mean ± SEM, *p <0.05 by unpaired t-test.

Fig. 5. Cell type-specific aging signatures in vestibular HCs. **(A)** PCA analysis of young and old type I and II HC from the 5 biological replicates. DESeq2 in Seurat was used with the default Wald test, and multiple testing was corrected using the Benjamini-Hochberg method. Variance stabilizing transformation (VST) was applied to assess the variance among different conditions. **(B)** Venn diagram indicating the number of shared and unique genes expressed in type I and II HCs. **(C)** Heatmaps of young and old type I and II HCs indicating top 50 DEGs. Rows represent genes, columns represent single cells, with expression levels ranging from high (purple) to low (yellow), p<0.05, FCcutoff - 0.25, log2FC. threshold - 0.1. **(D)** Volcano plots of young and old type I and II HCs, p<0.05, FCcutoff - 0.25, logfc. threshold - 0.1. The x-axis represents the log2 fold-change values (avg_log2FC). The y-axis represents the raw p-values (p_val). Wilcoxon rank-sum test with Bonferroni correction for false discovery FDR<0.01 was used to analyze DEGs. **(E)** Dot plots indicating some of the key downregulated genes identified from the DEG analysis. The dot size represents the percentage of cells expressing the genes from HC type I and II clusters, whereas the color indicates the expression level. Expression levels are normalized via z-score normalization. Thus, the average expression is zero, and positive or negative values indicate expression above or below average.

Fig. 6. Biological processes associated with old vestibular HCs. (A) GO enrichment analysis of the biological process (BP) (left) and Molecular function (MF) (right). The Hypergeometric test with the Benjamini-Hochberg adjustment was used. Pairwise semantic similarity was computed for clustering the GO terms, p-value < 0.05. **(B)** Circular network (CNET) plot illustrates genes associated with the downregulated biological processes. **(C)** Dot plots indicate the genes related to kinocilia. The dot size represents the percentage of cells expressing the genes from the HC cluster, whereas the color indicates the expression level. Expression levels are normalized via z-score normalization. Thus, the average expression is zero, and positive or negative values indicate expression above or below average. **(D)** KEGG pathway analysis of old vestibular HCs. The Hypergeometric test with the Benjamini-Hochberg p adjustment was used, p-value<0.05. (**E)** Enrichment of AD, PD, HD, ALS, and dementia susceptibility genes in vestibular HCs.

Fig. 7. Age-related reduction of key hair bundle markers and HC function. (A) RNAscope *in situ* hybridization validations of key HC genes identified from DEG and GO analysis in young and old otoliths and crista. Scale bar, 10 µm. **(B)** Dot plot shows the average gene expression levels in young and old HCs. **(C)** Quantifications of RNAscope *in situ* hybridization from otoliths (n=3) and crista (n=2). Data shown as mean ± SEM, ns-non-significant, *p <0.05, **p <0.01, ***p <0.001 by unpaired t-test. **(D)** Representative images depicting age-related reduction in stereocilia-related (ESPN) and kinocilia-related (CCDC39, CCDC40) markers (red) and quantifications of relative mean fluorescence intensity (n=3). Scale bar, 10 µm. Data are shown as mean ± SEM, ***p<0.001, ****p<0.0001 by unpaired t-test. **(E)** Representative images (utricle) and quantification of relative mean fluorescence intensity of FM1-43 dye uptake in young and old HCs in the utricle and cristae (n=3). Scale bar, 10 µm. Data are shown as mean ± SEM, **p <0.01, ***p <0.001 by unpaired t-test. **(F)** Representative images of vestibular microphonic measurements from young and old macula of the utricle (n=5 per age group). The stimulus was a 390 Hz sinusoid signal from a Burleigh PZ-150M Driver.

Fig. 8. Age-related changes in cochlear and vestibular HCs. (A) GO analysis showing biological processes downregulated in the old cochlear HCs compared to old vestibular HCs. The top genes that were downregulated in old cochlear HCs compared to age-matched old vestibular HCs were (Log2FC<0) used for this analysis using the Hypergeometric test with the Benjamini-Hochberg p adjustment, p<0.05. Pairwise semantic similarity was computed to cluster the GO terms. **(B)** RNAscope *in situ* hybridization validations and quantifications in cochlear HCs (n=3). Scale bar, 10 µm. Puncta density was quantified for each gene using FIJI (n=3). Data shown as mean ± SEM, ns-non-significant, *p <0.05, **p <0.01 by unpaired t-test. **(C)** Age-related Log2 fold changes of key genes related to HC functions in cochlear and vestibular HCs. **(D)** Senescence-associated β-galactosidase (SA-β-gal) activity at pH 6.0 in the cochlear and vestibular sensory epithelia with aging, indicating cellular senescence.

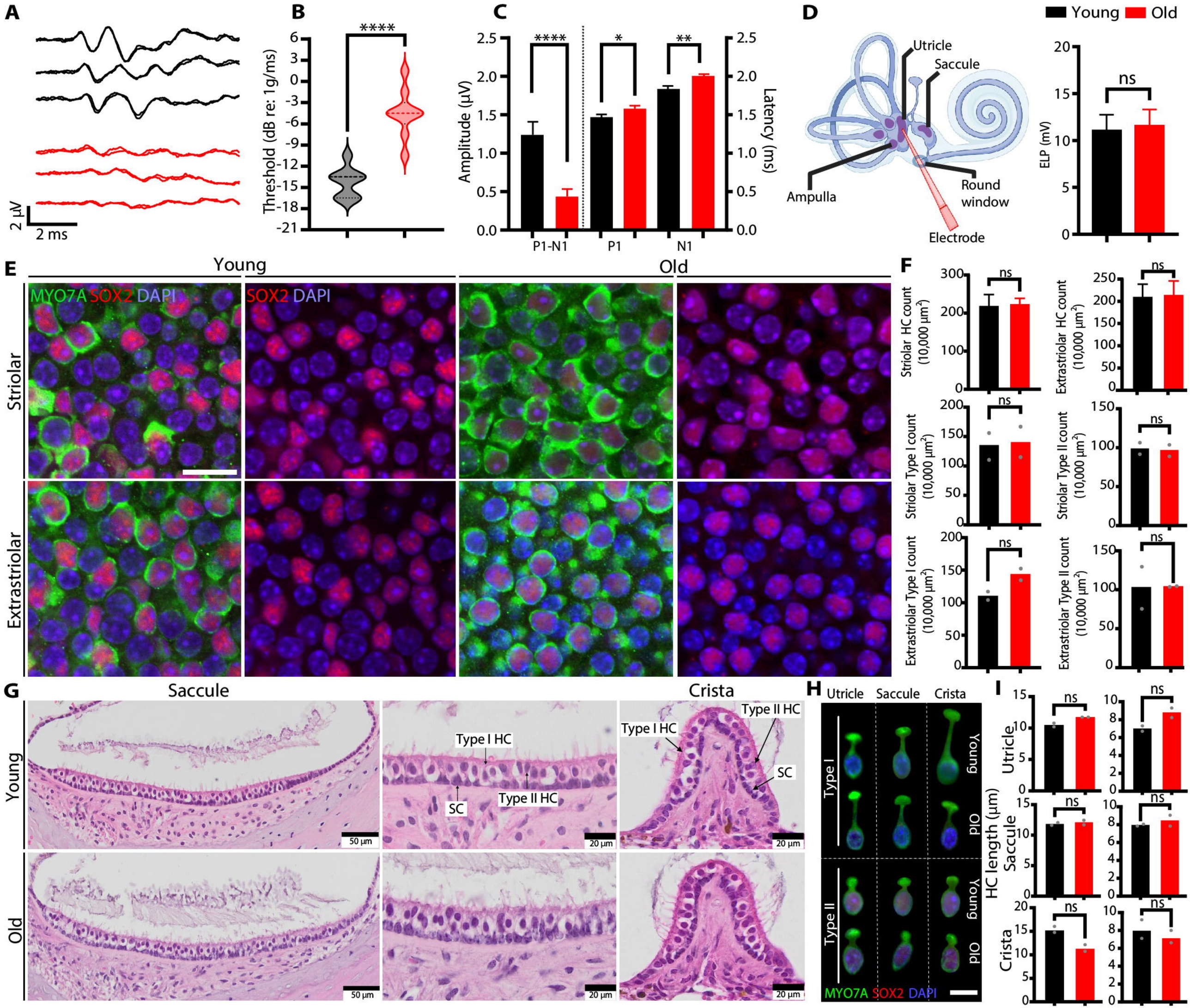
A
2 µV
2 ms
B
****
Threshold (dB re: 1g/ms)
6
3
0
-3
-6
-9
-12
-15
-18
-21
C
****
*
**
Amplitude (µV)
Latency (ms)
2.5
2.0
1.5
1.0
0.5
0.0
P1-N1
P1
N1
D
Young
Old
Utricle
Saccule
Ampulla
Round window
Electrode
ns
ELP (mV)
20
15
10
5
0
E
Young
Old
Striolar
Extrastriolar
MYO7A SOX2 DAPI
SOX2 DAPI
F
ns
Striolar HC count (10,000 µm²)
Extrastriolar HC count (10,000 µm²)
Striolar Type I count (10,000 µm²)
Striolar Type II count (10,000 µm²)
Extrastriolar Type I count (10,000 µm²)
Extrastriolar Type II count (10,000 µm²)
G
Saccule
Crista
Young
Old
Type I HC
Type II HC
SC
50 µm
20 µm
H
Utricle
Saccule
Crista
Type I
Type II
Young
Old
MYO7A SOX2 DAPI
I
ns
HC length (µm)
Utricle
Saccule
Crista

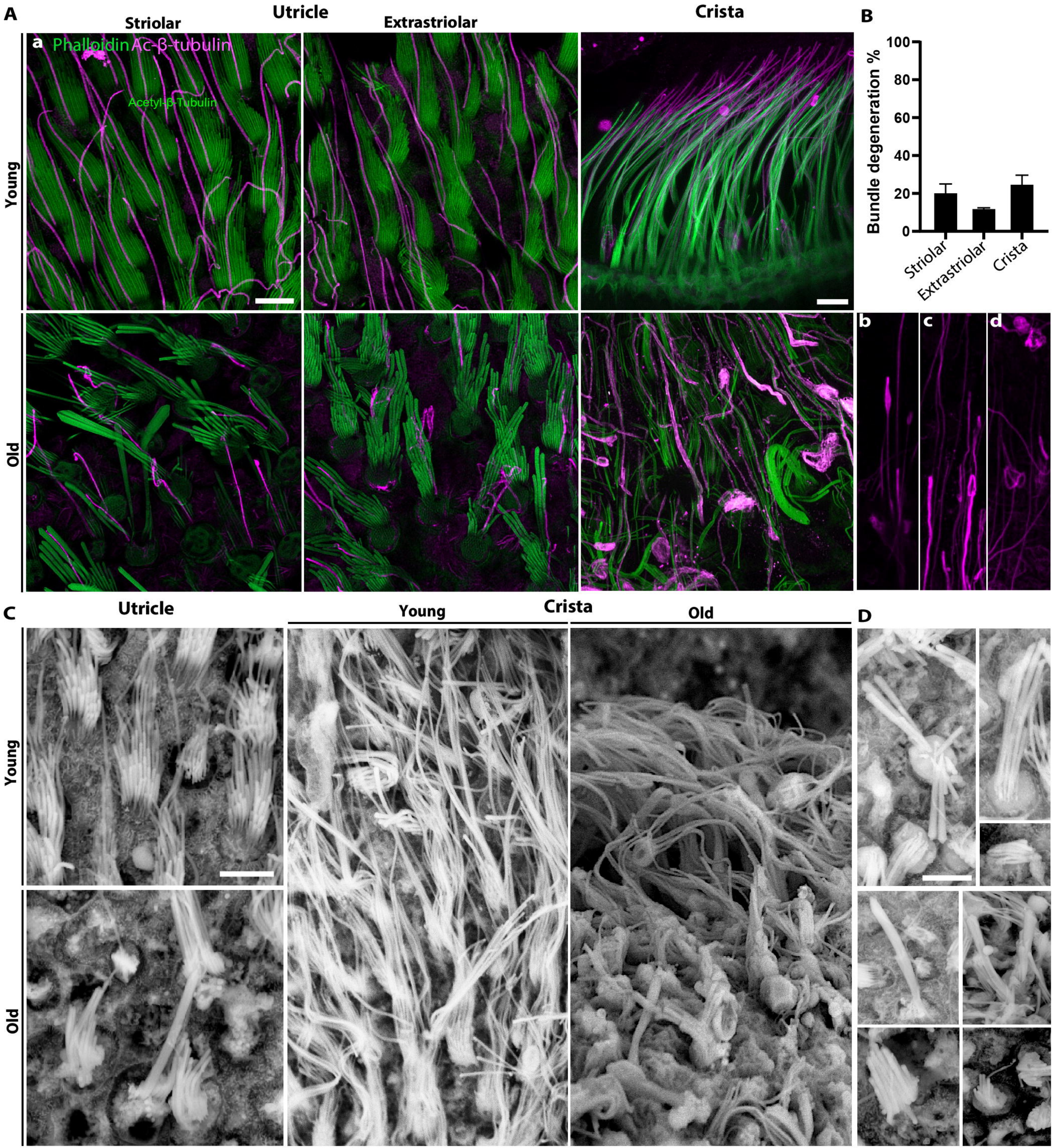
A
Utricle
Striolar
Extrastriolar
Crista
a
Phalloidin Ac-β-tubulin
Acetyl-β-Tubulin
Young
Old
B
Bundle degeneration %
100
80
60
40
20
0
Striolar
Extrastriolar
Crista
b
c
d
C
Utricle
Crista
Young
Old
Young
Old
D

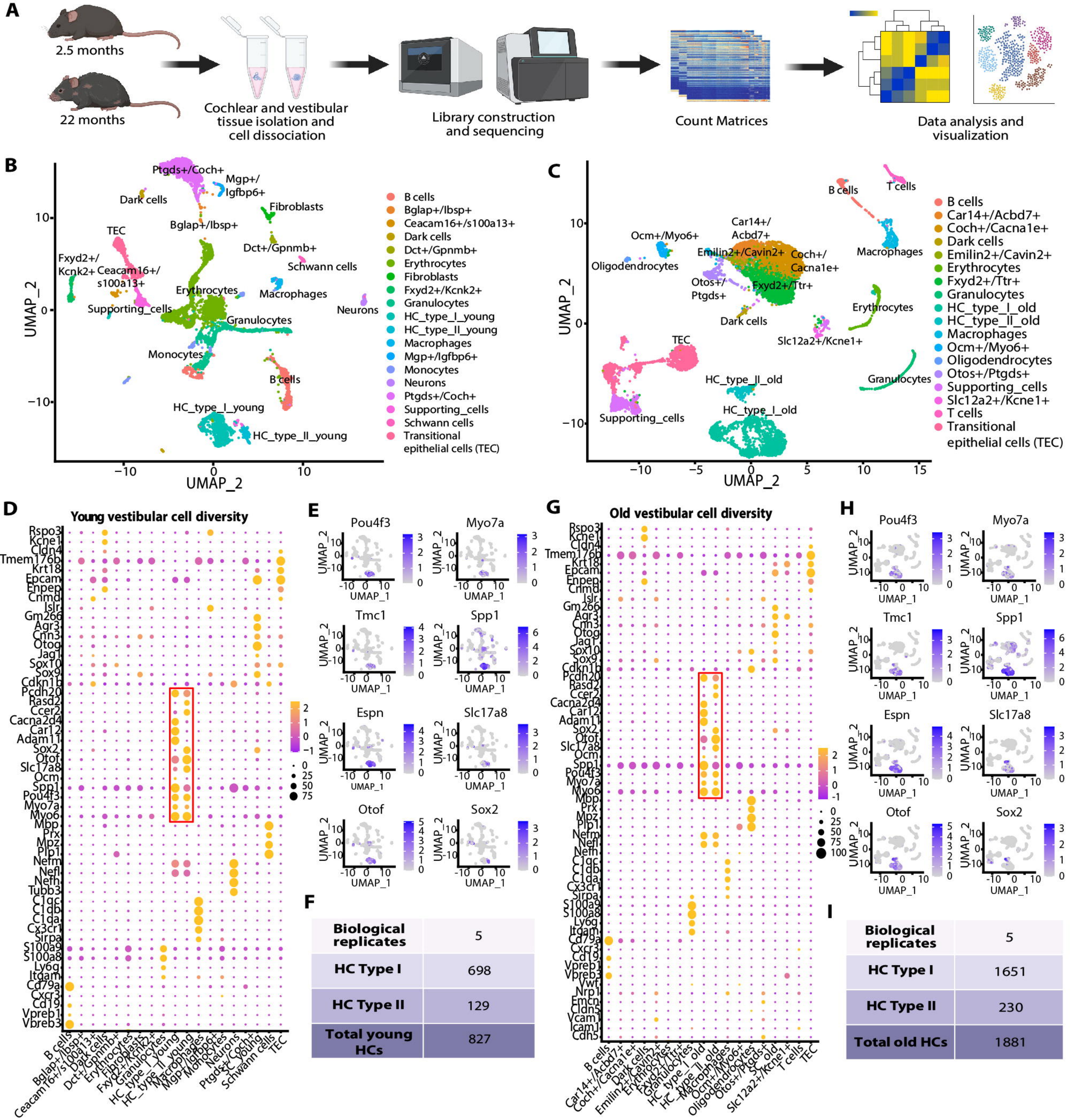

Biological replicates	5
HC Type I	698
HC Type II	129
Total young HCs	827

Biological replicates	5
HC Type I	1651
HC Type II	230
Total old HCs	1881

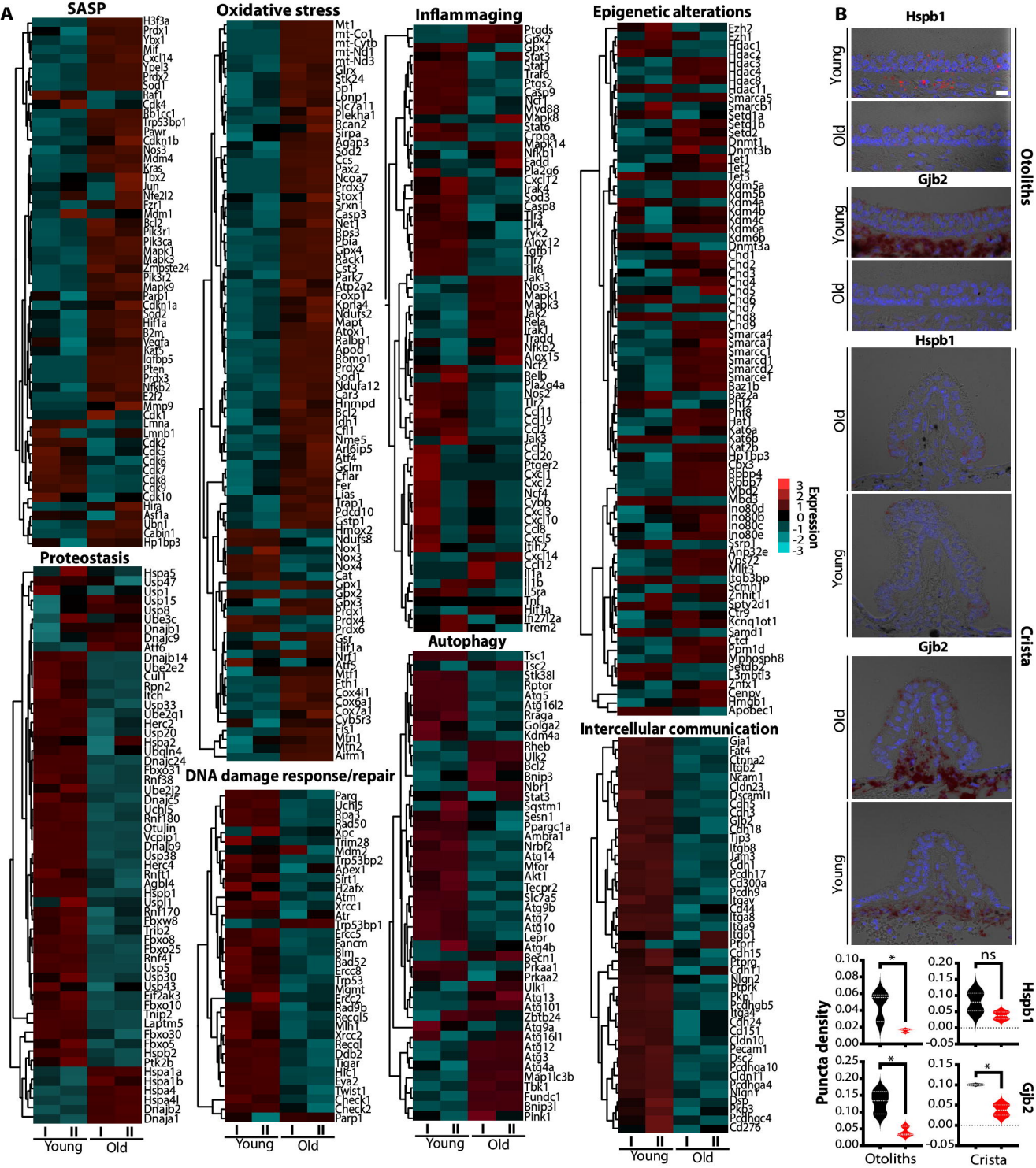
A
SASP
H3f3a
Prdx1
Ybx1
Mif
Cxcl14
Ypel3
Prdx2
Sod1
Raf1
Cdk4
Rb1cc1
Trp53bp1
Pawr
Cdkn1b
Nos3
Mdm4
Kras
Tbx2
Jun
Nfe2l2
Fzr1
Mdm1
Bcl2
Pik3r1
Pik3ca
Mapk1
Mapk3
Zmpste24
Pik3r2
Mapk9
Parp1
Cdkn1a
Sod2
Hif1a
B2m
Vegfa
Kat5
Igfbp5
Pten
Prdx3
Nfkb2
E2f2
Mmp9
Cdk1
Lmna
Lmnb1
Cdk2
Cdk5
Cdk6
Cdk7
Cdk8
Cdk9
Cdk10
Hira
Asf1a
Ubn1
Cabin1
Hp1bp3
Oxidative stress
Mt1
mt-Co1
mt-Cyb
mt-Nd1
mt-Nd3
Glrx
Stk24
Sp1
Lonp1
Slc7a11
Plekha1
Rcan2
Sirpa
Agap3
Sod1
Ccs
Pax2
Ncoa7
Prdx3
Stox1
Srxn1
Casp3
Net1
Bps3
Pbia
Gpx4
Rack1
Cst3
Park7
Atp2a2
Foxp1
Kpna4
Ndufs2
Mapt
Atox1
Ralbp1
Apod
Romo1
Prdx2
Sod1
Ndufa12
Ar3
Hnrnpd
Bcl2
Idh1
Ctl1
Nme5
Arl6ip5
Atf4
Gclm
Cflar
Fer
Lias
Trap1
Pdcd10
Gstp1
Hmox2
Ndufs8
Nox1
Nox3
Nox4
Cat
Gpx1
Gpx2
Gpx3
Prdx1
Prdx4
Prdx6
Gsr
Hif1a
Nrf1
Atf5
Mtf1
Fth1
Cox4i1
Cox6a1
Cox7a1
Cyb5r3
Fis1
Mfn1
Mfn2
Aifm1
Inflammaging
Ptgds
Gpx2
Gpx1
Stat3
Stat1
Traf6
Ptgs2
Casp9
Ncf
Myd88
Mapk8
Stat6
Crpna
Mapk14
Nfkb1
Fadd
Pla2g6
Cxcl12
Irak4
Sod3
Casp8
Tlr3
Tlr4
Tyk2
Alox12
Igfb1
Tlr7
Tlr8
Jak1
Nos3
Map4k1
Mapk3
Jak2
Rela
Irak1
Tradd
Nfkb2
Alox15
Ncf2
Relb
Pla2g4a
Nos2a
Tlr2
Ccl11
Ccl19
Ccl2
Jak3
Ccl5
Ccl20
Ptger2
Cxcl1
Cxcl2
Ncf4
Cybb
Cxcl3
Cxcl10
Ccl8
Cxcl5
Il1rl2
Cxcl14
Ccl12
Il1a
Il1b
Il5ra
Tnf
Hif1a
Il27l2a
Trem2
Epigenetic alterations
Ezh2
Ezh1
Hdac1
Hdac2
Hdac3
Hdac4
Hdac8
Hdac11
Smarca5
Smarcb1
Setd1a
Setd1b
Setd2
Dnmt1
Dnmt3b
Tet1
Tet2
Tet3
Kdm5a
Kdm5b
Kdm4a
Kdm4b
Kdm4c
Kdm6a
Kdm6b
Dnmt3a
Chd1
Chd2
Chd3
Chd4
Chd5
Chd6
Chd7
Chd8
Chd9
Smarca4
Smarca1
Smarcc1
Smarcd1
Smarcd2
Smarce1
Baz1b
Baz2a
Phf2
Phf8
Hat1
Kat6a
Kat6b
Kat2b
Hp1bp3
Cbx3
Rbbp4
Rbbp7
Mbd2
Mbd3
Ino80d
Ino80b
Ino80c
Ino80e
Ssrp1
Anp32e
Vps72
Mllt3
Itgb3bp
Scmh1
Znhit1
Spty2d1
Ctr9
Kcnq1ot1
Samd1
Ctcf
Ppm1d
Mphosph8
Setdb2
L3mbtl3
Znfx1
Cenpv
Hmgb1
Apobec1
Intercellular communication
Gja1
Fat4
Ctnna2
Itgb2
Ncam1
Cldn23
Dscaml1
Cdh3
Cdh3
Gjb2
Cdh18
Tjp3
Itgb8
Jam3
Cdh1
Pcdh17
Cd300a
Pcdh9
Itgav
Cd44
Itga8
Itga9
Itdb1
Ptprf
Cdh15
Ptprg
Cdh1
Nlgn2
Ptprk
Pkp1
Pcdhgb5
Itga4
Cd24
Cd151
Cldn10
Pecam1
Dsg3
Pcdhga10
Cldn11
Pcdhga4
Nlgn1
Pkp3
Pcdhgc4
Cd276
Proteostasis
Hspa5
Usp47
Usp1
Usp15
Usp8
Ube3c
Dnajb1
Dnajc9
Atf6
Dnajb14
Ube2e2
Cul1
Rpn2
Itch
Usp33
Ube2q1
Herc2
Usp20
Hspa2
Ubqln4
Dnajc24
Fbxo31
Rnf38
Ube2j2
Dnajc5
Uchl5
Rnf180
Otulin
Vcpip1
Dnajb9
Usp38
Herc4
Rnft1
Agbl4
Hspb1
Usp1
Rnf170
Fbxw8
Trib2
Fbxo8
Fbxo25
Rnf41
Usp5
Usp30
Usp43
Eif2ak3
Fbxo10
Tnip2
Laptm5
Fbxo30
Fbxo5
Hspb2
Ptk2b
Hspa1a
Hspa1b
Hspa4
Hspa4l
Dnajb2
Dnaja1
DNA damage response/repair
Parg
Uchl5
Rpa3
Rad50
Xpc
Trim28
Mdm2
Trp53bp2
Apex1
Sirt1
H2afx
Atm
Xrcc1
Atr
Trp53bp1
Ercc5
Fancm
Blm
Rad52
Ercc8
Trp53
Mgmt
Ercc2
Rad9b
Recql5
Mlh1
Xrcc2
Recql
Ddb2
Tigar
Hic1
Eya2
Twist1
Chek1
Chek2
Parp1
Autophagy
Tsc1
Tsc2
Stk38l
Rptor
Atg5
Atg16l2
Rraga
Golga2
Kdm4a
Rheb
Ulk2
Bcl2
Bnip3
Nbr1
Stat3
Sqstm1
Sesn1
Ppargc1a
Ambra1
Nrbf2
Atg14
Mtor
Akt1
Tecpr2
Slc7a5
Atg9b
Atg7
Atg10
Lepr
Atg4b
Becn1
Prkaa1
Prkaa2
Ulk1
Atg13
Atg101
Zbtb24
Atg9a
Atg16l1
Atg12
Atg3
Atg4a
Map1lc3b
Tbk1
Fundc1
Bnip3l
Pink1
Young
Old
Expression
3
2
1
0
-1
-2
-3
B
Hspb1
Gjb2
Young
Old
Otoliths
Crista
Puncta density
ns
*
Otoliths
Crista

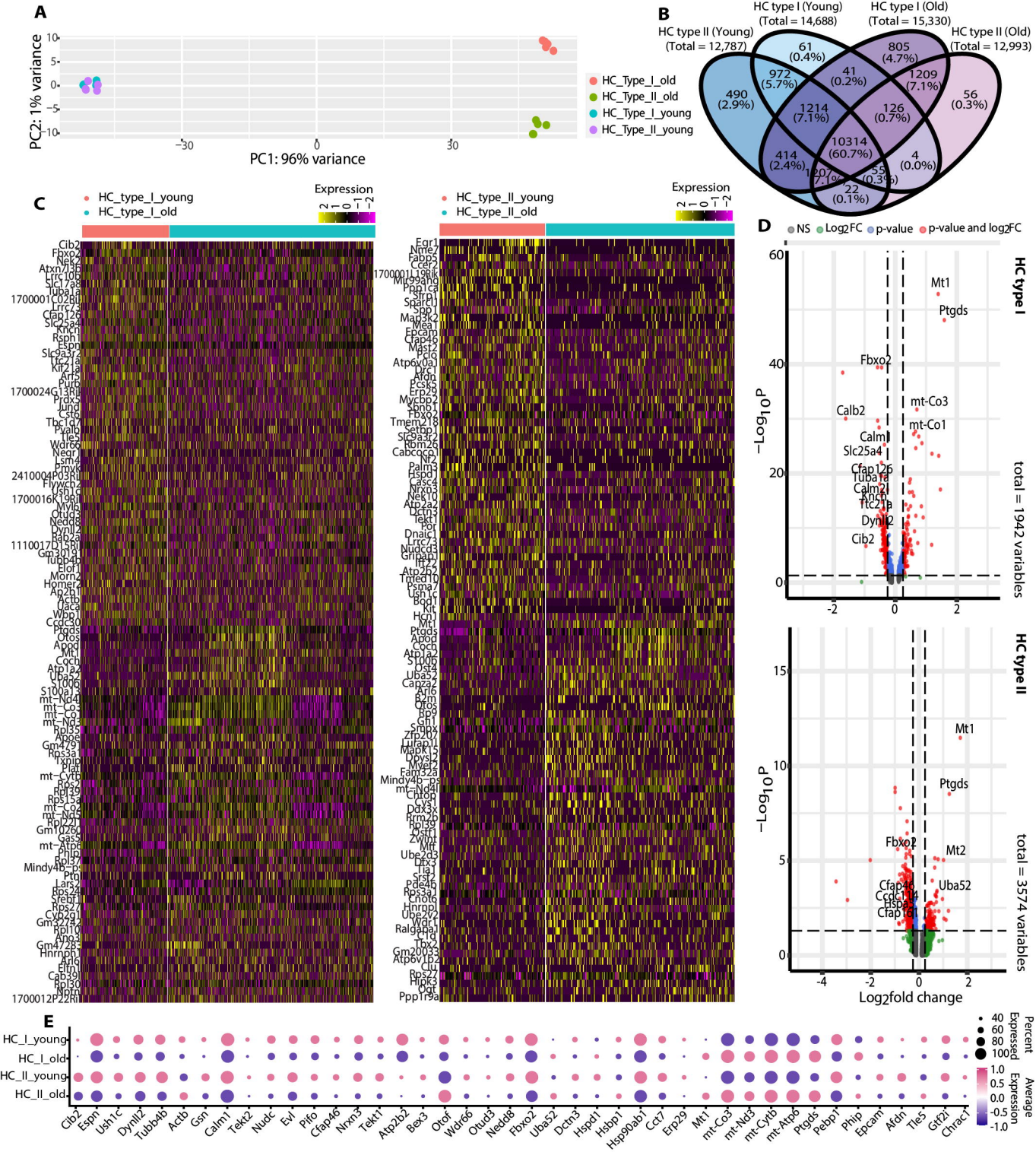
A
PC2: 1% variance
PC1: 96% variance
HC_Type_I_old
HC_Type_II_old
HC_Type_I_young
HC_Type_II_young
B
HC type I (Young) (Total = 14,688)
HC type I (Old) (Total = 15,330)
HC type II (Young) (Total = 12,787)
HC type II (Old) (Total = 12,993)
61 (0.4%)
805 (4.7%)
972 (5.7%)
41 (0.2%)
1209 (7.1%)
490 (2.9%)
1214 (7.1%)
126 (0.7%)
56 (0.3%)
10314 (60.7%)
414 (2.4%)
4 (0.0%)
1207 (7.1%)
55 (0.3%)
22 (0.1%)
C
HC_type_I_young
HC_type_I_old
HC_type_II_young
HC_type_II_old
Expression
D
NS
Log2FC
p-value
p-value and log2FC
HC type I
total = 1942 variables
HC type II
total = 3574 variables
−Log10P
Log2fold change
E
HC_I_young
HC_I_old
HC_II_young
HC_II_old
Percent Expressed
Average Expression

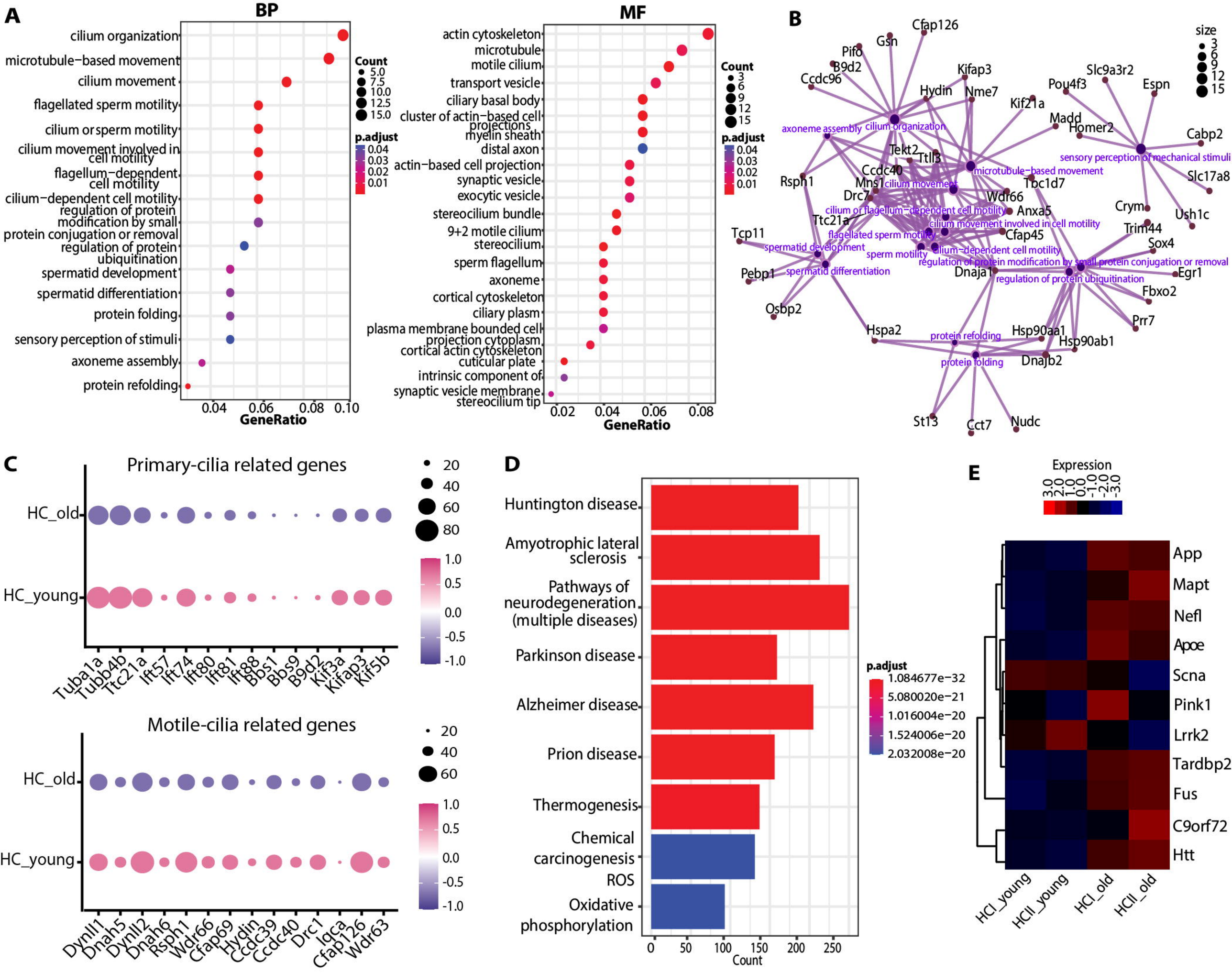
A
BP
cilium organization
microtubule−based movement
cilium movement
flagellated sperm motility
cilium or sperm motility
cilium movement involved in cell motility
flagellum−dependent cell motility
cilium−dependent cell motility
regulation of protein modification by small protein conjugation or removal
regulation of protein ubiquitination
spermatid development
spermatid differentiation
protein folding
sensory perception of stimuli
axoneme assembly
protein refolding
0.04 0.06 0.08 0.10
GeneRatio
Count
5.0 7.5 10.0 12.5 15.0
p.adjust
0.04 0.03 0.02 0.01
MF
actin cytoskeleton
microtubule
motile cilium
transport vesicle
ciliary basal body
cluster of actin−based cell projections
myelin sheath
distal axon
actin−based cell projection
synaptic vesicle
exocytic vesicle
stereocilium bundle
9+2 motile cilium
stereocilium
sperm flagellum
axoneme
cortical cytoskeleton
ciliary plasm
plasma membrane bounded cell projection cytoplasm
cortical actin cytoskeleton
cuticular plate
intrinsic component of synaptic vesicle membrane
stereocilium tip
0.02 0.04 0.06 0.08
GeneRatio
Count
3 6 9 12 15
p.adjust
0.04 0.03 0.02 0.01
B
size
3 6 9 12 15
Cfap126
Gsn
Pifo
B9d2
Ccdc96
Kifap3
Hydin
Nme7
Slc9a3r2
Pou4f3
Espn
Kif21a
Madd
Homer2
Cabp2
axoneme assembly
cilium organization
Tekt2
Ttll3
sensory perception of mechanical stimuli
Slc17a8
Ccdc40
microtubule−based movement
Rsph1
Mns1
cilium movement
Tbc1d7
Drc7
Wdr66
Crym
Ush1c
cilium or flagellum−dependent cell motility
Anxa5
Ttc21a
cilium movement involved in cell motility
Trim44
Tcp11
flagellated sperm motility
Cfap45
Sox4
spermatid development
sperm motility
cilium−dependent cell motility
regulation of protein modification by small protein conjugation or removal
Pebp1
spermatid differentiation
Dnaja1
Egr1
regulation of protein ubiquitination
Fbxo2
Osbp2
Prr7
Hspa2
protein refolding
Hsp90aa1
Hsp90ab1
protein folding
Dnajb2
St13
Cct7
Nudc
C
Primary-cilia related genes
HC_old
HC_young
Tuba1a Tubb4b Ttc21a Ift57 Ift74 Ift80 Ift81 Ift88 Bbs1 Bbs9 B9d2 Kif3a Kifap3 Kif5b
20 40 60 80
1.0 0.5 0.0 -0.5 -1.0
Motile-cilia related genes
HC_old
HC_young
Dynll1 Dnah5 Dynll2 Dnah6 Rsph1 Wdr66 Cfap69 Hydin Ccdc39 Ccdc40 Drc1 Iqca Cfap126 Wdr63
20 40 60
1.0 0.5 0.0 -0.5 -1.0
D
Huntington disease
Amyotrophic lateral sclerosis
Pathways of neurodegeneration (multiple diseases)
Parkinson disease
Alzheimer disease
Prion disease
Thermogenesis
Chemical carcinogenesis ROS
Oxidative phosphorylation
0 50 100 150 200 250
Count
p.adjust
1.084677e−32
5.080020e−21
1.016004e−20
1.524006e−20
2.032008e−20
E
Expression
3.0 2.0 1.0 0.0 -1.0 -2.0 -3.0
App
Mapt
Nefl
Apoe
Scna
Pink1
Lrrk2
Tardbp2
Fus
C9orf72
Htt
HCI_young
HCII_young
HCI_old
HCII_old

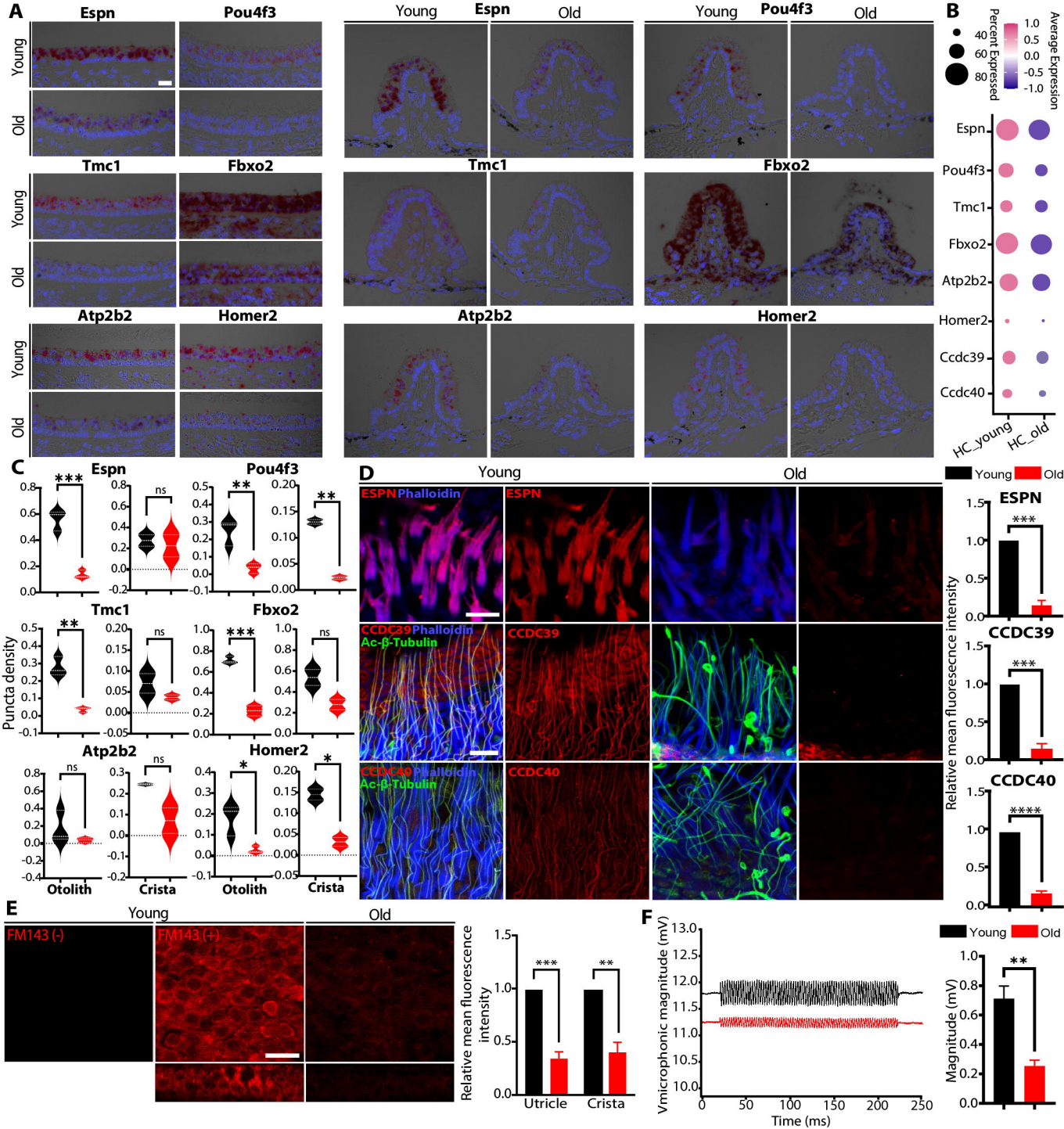
A
Espn
Pou4f3
Young
Old
Tmc1
Fbxo2
Atp2b2
Homer2
B
Percent Expressed
Average Expression
Ccdc39
Ccdc40
HC_young
HC_old
C
Puncta density
Otolith
Crista
D
ESPN Phalloidin
CCDC39 Phalloidin Ac-β-Tubulin
CCDC40 Phalloidin Ac-β-Tubulin
Relative mean fluorescence intensity
E
FM143 (-)
FM143 (+)
Relative mean fluorescence intensity
Utricle
F
Vmicrophonic magnitude (mV)
Time (ms)
Magnitude (mV)

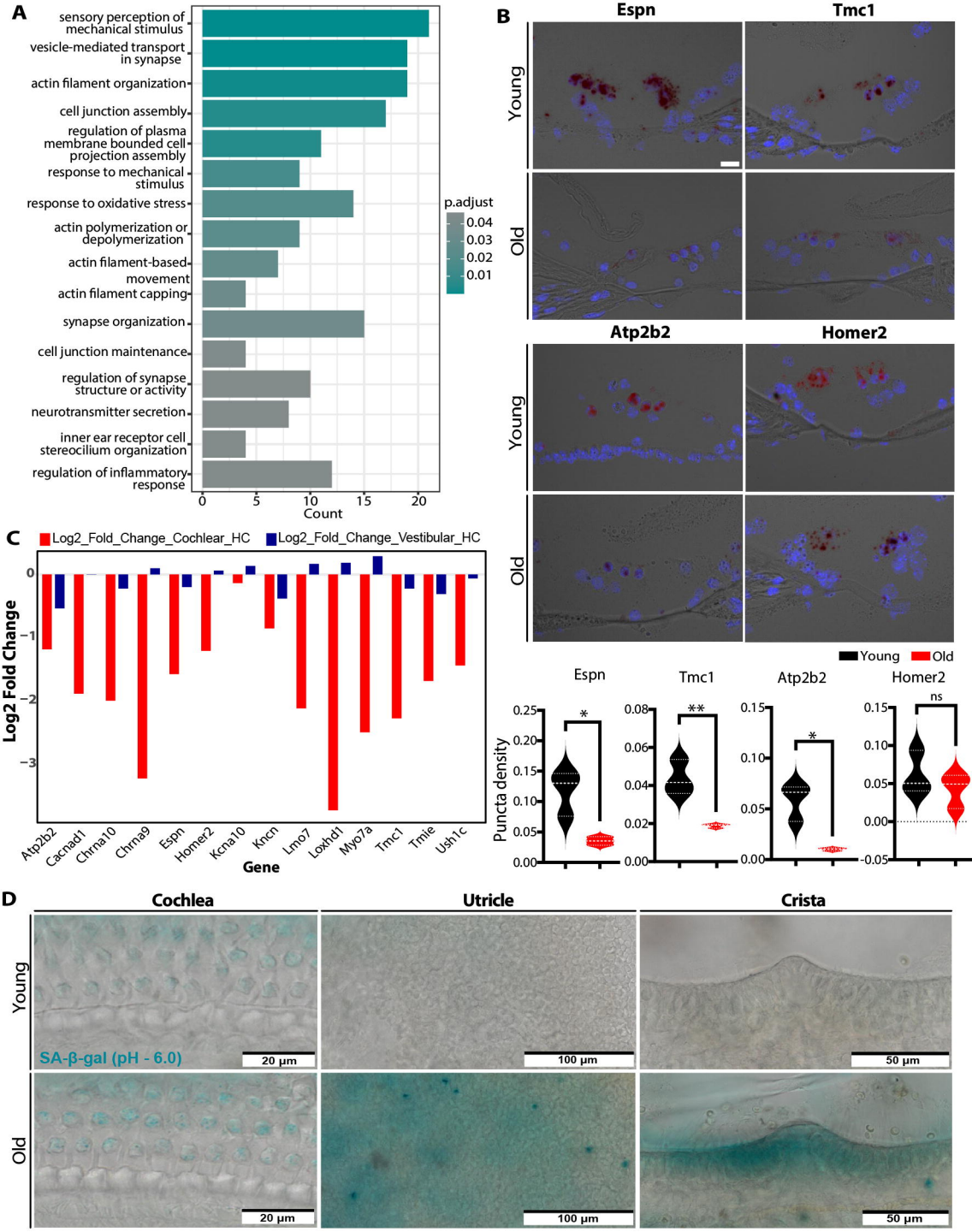
A
sensory perception of mechanical stimulus
vesicle-mediated transport in synapse
actin filament organization
cell junction assembly
regulation of plasma membrane bounded cell projection assembly
response to mechanical stimulus
response to oxidative stress
actin polymerization or depolymerization
actin filament-based movement
actin filament capping
synapse organization
cell junction maintenance
regulation of synapse structure or activity
neurotransmitter secretion
inner ear receptor cell stereocilium organization
regulation of inflammatory response
0
5
10
15
20
Count
p.adjust
0.04
0.03
0.02
0.01
B
Espn
Tmc1
Young
Old
Atp2b2
Homer2
Young
Old
Young
Old
Espn
Tmc1
Atp2b2
Homer2
Puncta density
*
**
*
ns
C
Log2_Fold_Change_Cochlear_HC
Log2_Fold_Change_Vestibular_HC
Log2 Fold Change
0
−1
−2
−3
Atp2b2
Cacnad1
Chrna10
Chrna9
Espn
Homer2
Kcna10
Kncn
Lmo7
Loxhd1
Myo7a
Tmc1
Tmie
Ush1c
Gene
D
Cochlea
Utricle
Crista
Young
Old
SA-β-gal (pH - 6.0)
20 μm
100 μm
50 μm
20 μm
100 μm
50 μm